

Uni-Fusion: Universal Continuous Mapping

Yijun Yuan and Andreas Nüchter

Abstract—We introduce Uni-Fusion, an universal continuous mapping framework for surfaces, surface properties (color, infrared, etc.) and more (latent features in CLIP embedding space, etc.). We propose the first Universal Implicit Encoding model that supports encoding of both geometry and various types of properties (RGB, infrared, feature and etc.) without the need for any training. Based on that, our framework divides the point cloud into regular grid voxels and produces a latent feature in each voxel to form a Latent Implicit Map (LIM) for geometries and arbitrary properties. Then, by fusing a Local LIM of new frame to Global LIM, an incremental reconstruction is approached. Encoded with corresponding types of data, our Latent Implicit Map is capable to generate continuous surfaces, surface properties fields, surface feature fields and any other possible options. To demonstrate the capabilities of our model, we implement three applications: (1) incremental reconstruction for surfaces and color (2) 2D-to-3D fabricated properties transfers (3) open-vocabulary scene understanding by producing a text CLIP feature field on surfaces. We evaluate Uni-Fusion by comparing in corresponding applications, from which, Uni-Fusion shows high flexibility to various of application while performing best or competitive. The project page of Uni-Fusion is available at <https://jarrome.github.io/Uni-Fusion/>

Index Terms—Mapping, RGB-D perception, Semantic scene understanding, Universal mapping

I. INTRODUCTION

For robotics, 3D perception is crucial for robots to perform interaction with the surroundings. Operating different types of sensors and perform reconstructions and scene understandings are essential to 3D perception. In those tasks, various properties information need to be considered, such as geometry and surface properties. However, algorithms have to be accordingly design.

So in this beginning, we post **one question**: *Is it possible to address all those information with one universal mapping model?*

Reconstruction, as one of the most blossom topic in field, has been developed for decades. During which, batches of works pushed the limits [1]–[14]. Given a set of points, reconstruction models aim to extract the zero-level surface. Those approaches are usually based on occupancy fields and signed distance functions (SDFs). Occupancy field are more used in 2D and objective-level shape reconstruction, where Gaussian Process Occupancy Maps (GPOM), Gaussian Process Implicit Surface (GPIS) and Hilbert Maps are invented to produce continuous probabilistic occupancy maps. For scene-level reconstruction, most recent works rely on Signed Distance Fields. TSDF-Fusion [8], as the most widely used reconstruction model, paved the way for real-time 3D reconstruction. With the fast developemt of RGB-D sensors, such as the Kinect

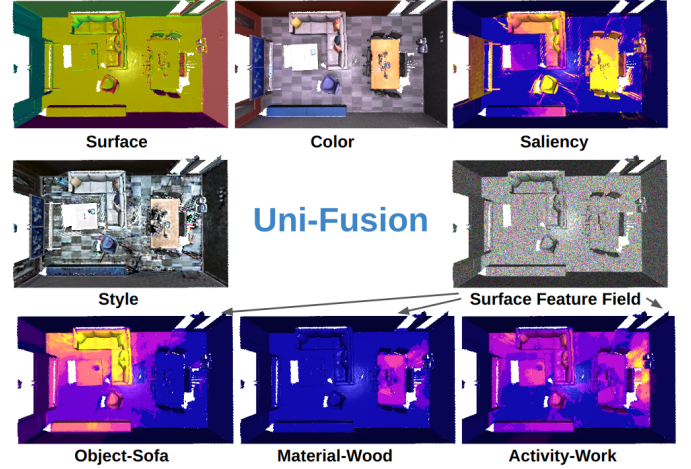


Fig. 1. One Universal Continues Mapping for all reconstructions. Such as surface, properties including RGB, saliency, style and ..., even high dimensional features (CLIP embeddings, and etc).

or RealSense series, standard models have been invented [9], [10]. These models utilize discretized Signed Distance Fields (SDFs) and the Marching Cubes algorithm [15].

To cope the high demand of memory consumption of such representation, recent techniques relies on Deep Neural Networks for encoding the geometry [11], [12], [14], [16].

Using a sparse grid of local clusters, high dimensional vectors are extracted for each cluster. With such a representation, researchers have proposed the fusion on the map of latent vectors instead of the explicit field. The explicit field is then extracted with arbitrary resolution. Thus, such form of representation produces a continuous mapping. Those methods are called Neural Implicit Maps (NIMs).

Encoding functions for recent NIM techniques using a pre-trained model from objective datasets were shown in [11], [12], [16]. It becomes impossible to pre-train for context of color or other point properties, since the context pattern, like color, is much more complex than shape. The only recent solution for continuous color reconstruction are based on back-propagation of local latent features [14] or using Neural Radiance Fields (NeRF) [17]. However, those methods requires adequate epochs to train and are not capable for real-time. Thus, in this paper aims to fill the gap: We propose a universal model that encodes arbitrary properties directly without any time-consuming learning (and training).

Our model is based on Gaussian Process Regression (GPR). Trained from nothing, we propose to approximate kernels and thus are able to decouple the GPR to reduce the point cluster to one feature vector. Then relies on the sparse voxel structure, we build such feature vector locally in each voxel to form a map of latents. Because our encoding-decoding function is

The authors are with Informatics XVII – Robotics at Julius-Maximilians-University of Würzburg, Germany. {yijun.yuan|andreas.nuechter}@uni-wuerzburg.de

with GPR, the whole model does not pre-touch any format of data properties. Thus, our Uni-Fusion is applicable to arbitrary reconstruction applications.

We consider that there does not exist such a model to operate all types of data for all perception needs of robot. Therefore, based on that encoder, we introduce Uni-Fusion, a universal model for all types of data, that produces continuous maps. A selected set of examples of “what Uni-Fusion can do” is shown in Fig. 1. Given various types of input data, our Uni-Fusion is capable to encode and produce continuous maps for surfaces, color, styles, and more. To better explore the potential of such a model, we even construct an field for high dimensional CLIP-embedding [18].

The contribution of this paper are as follows:

- we propose an universal encoding-decoding model for local information that does not require any training,
- we introduce the first universal continuous mapping model for construction of continuous surfaces and various surface property fields, even for high dimensional features, such as CLIP-embeddings.
- we implement applications to demonstrate the capabilities: (1) Incremental surface & color reconstruction, (2) 2D-to-3D transfer on 3D canvas, (3) open-vocabulary scene understanding.

Content Overview: In the following we review related works (Section II). We first introduce the continues mapping developed from 2D scenes to 3D scenes. Then we discuss about the importance of recent state-of-the-art (SOTA) of neural implicit-based reconstructions. Then, we introduce the development of Kernel methods where our method is belonging to. Afterwards, in Section III and Section IV, we respectively introduce the universal encoder and the universal continuous mapping model Uni-Fusion that based on such a encoder. Finally, in Section V, we implement a series of applications to demonstrate the wide applicability of Uni-Fusion in various scenarios. The evaluation of Uni-Fusion is given in Section VI to demonstrate its high capabilities. In the end, we describe the future work of the Uni-Fusion project and conclude the paper.

II. RELATED WORKS

A. Continues Mapping

Continuous Mapping started with 2D scenarios. Gaussian Process Occupancy Maps (GPOM) [1] first uses Gaussian Process Regression (GPR) to predict a continuous representation to enable the map construction at arbitrary resolution. Then, by borrowing the Bayesian Committee Machine (BCM) technique, incremental GPOM is approached [2], [3].

In the meanwhile, the Hilbert Maps approach [19], [20] were presented. Which is a mapping approach without an explicit formulation. Hilbert Maps perform continuous mapping by keeping optimizing parameters in the background.

With increasing popularity of 3D sensors, the focus shifted towards 3D cases. Gaussian Process Implicit Surface (GPIS), has entered the field [4]–[7]. Given zero-level surface points, those methods either sample points along normal direction and assign distance values or directly utilize derivative models

with normals as labels (we will give more detail in our mapping Section IV-B). However, those methods majorly work on shapes but not scenes. It is due to the fact, that GPR based methods naturely suffer under the high computational costs when large amount of data is involved. Especially when the test scope moves from 2D to 3D. Thus, we borrow the idea of Neural Implicit Maps (Section II-B) to address this issue and work on scene reconstruction.

B. Neural implicit based Reconstruction

Neural implicit reconstruction have orginally be introduced to SDF and Occupancy based reconstruction. The seminal work of [21], i.e., DeepSDF, utilizes deep model to encode geometry prior with Multi-layer perceptrons (MLPs) and extract discretized SDF by querying from decoding. Then, an algorithm similiar to Marching Cubes [15] is applied to extract meshes. For the latter, Occupancy Networks [22] learn to estimate the occupancy probability at positions from an implicit function. Meshes are generated with the Multiresolution IsoSurface Extraction (MISE) technique.

To improve the efficiency of the reconstruction, DeepLS [23] resorts to multiple local deep priors and reconstructs on a set of local SDFs. Jiang et al. [24] further proposes to utilize a local implicit grid that further eases the complexity of learning the encoding. In contrast, Convolutional Occupancy Networks [25] explore the local latent by replacing the encoder-decoder with optimization on a grid of local features to ease the burden of simple MLPs.

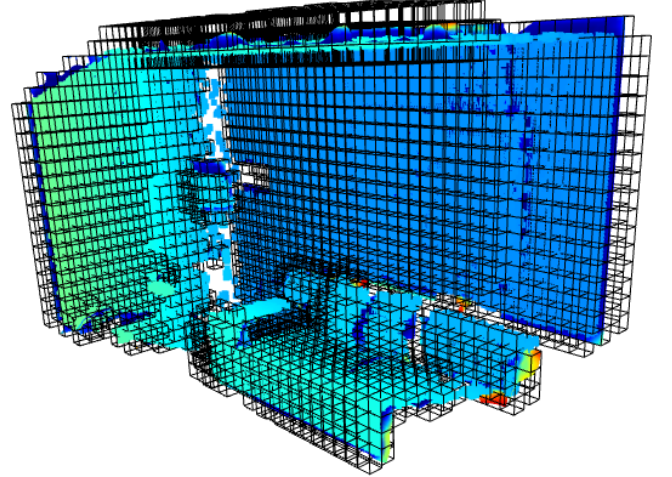


Fig. 2. Uniform, sparse voxels. Each voxel is encoded to one feature vector \mathbf{F}_m [11].

More recently, Neural Implicit Maps (NIM) achieve real-time real-scene 3D reconstruction. Huang et al. propose DI-Fusion [11], a neural implicit mapping method that incrementally reconstructs a scene. By fusing on maps of latent features, DI-Fusion achieves high efficiency of memory while yielding better reconstructions. Similarly, NeuralBlox [26] also fuse a grid of latent features given a known external pose estimation. To further improve the feature quality, BNV-Fusion [16] additionally add post-optimization after fusion. To handle large scene reconstructions, that may contain loops, NIM-REM [12]

proposes a SE(3)-transformation algorithm on NIM and implements a mapping&remapping model supporting working alongside Bundle Adjustment or SLAM with Loop-closing. Thinking outside of the box, Sucar et al. propose iMAP [13] a novel SLAM pipeline with neural implicit based incremental reconstruction. With a differentiable rendering model, iMAP is able to online optimize the reconstruction by minimizing the image distances. Zhu et al. presents NICE-SLAM [14], that replaces the MLPs with convolutional occupancy grid to further improve the efficiency and quality of the reconstruction.

In this work, our model also relies on the regular spaced voxels as in Fig. 2 for local encoding-decoding. Since we propose to use one model for all properties, it is not possible to pre-train such a model. Therefore, we rely on a kernel method to achieve this goal.

C. Kernel Function Approximation

Kernel methods are not scalable as the mapping from n points to a kernel requires $O(n^2)$ time complexity. One possible solution is with kernel matrix approximation but is not in the scope of this paper. The other solution, kernel function approximation, proposes to improve the scalability of kernel method using explicit vector maps. For example, $k(\mathbf{x}_1, \mathbf{x}_2) \approx \mathbf{v}(\mathbf{x}_1)^T \mathbf{v}(\mathbf{x}_2)$ with mapping function $\mathbf{v} : \mathbb{X} \rightarrow \mathbb{R}^l$ [27]. There are two approaches to address the approximation. One is Random Fourier Features (RFFs) [28]–[32] and the second is Nyström method [27], [32], [33].

RFFs explicitly handle the shift-invariant kernels by mapping the data using the Fourier transform technique [32]. However, RFFs are majorly used to handle shift-invariant kernels and maintain a large l . In addition, as RFFs are data independent, this leads to a significantly worse generalization performance than Nyström methods [34]. Differently, Nyström methods can be applied to approximate any positive-definite kernel [27]. It resorts to finding the eigenfunctions to form the approximation:

$$k(\mathbf{x}_1, \mathbf{x}_2) = \sum_{i \geq 1} \mu_i \varphi_i(\mathbf{x}_1) \varphi_i(\mathbf{x}_2),$$

where φ_i and $\mu_i \geq 0$ are eigenfunctions and eigenvalues of kernel $k(\mathbf{x}_1, \mathbf{x}_2)$ with respect to the probability measure q . With the top- l eigenpairs, the Nyström method approximate a kernel with $k(\mathbf{x}_1, \mathbf{x}_2) = \sum_{i \geq 1}^l \mu_i \varphi_i(x) \varphi_i(y)$.

However, Nyström methods are still costly on medium-sized training data and require N -times evaluation of each sample which is not efficient to direct regression of a continuous map.

We instead encode the local geometry and properties. This means a full space approximation is not necessary. By restricting the approximation to the limited space $\mathbf{x} \in [-0.5, 0.5]^3$, and applying the function in each local region, we overcome the high-computational burden.

III. DECOUPLED REGRESSION AS AN UNIVERSAL ENCODING

In this section, we propose an universal encoding model for point clouds. Based on this encoder, in Section IV, we introduce Universal Continuous Mapping.

A. Decoupled Gaussian Process Regression as Encoder-Decoder

Inspired by DI-Fusion [11] that introduces maps of latent features for continuous surface prediction, we aim to produce a latent vector for each local patch. Firstly, an universal encoder design comes from the Gaussian Process Regression (GPR) which is a widely used techniques for low dimensional regression. It has been utilized in various mapping models [3], [4]. Given a dataset with N observation points $\{(\mathbf{x}_n, \mathbf{y}_n)\}_{n=1}^N$ where point positions are $\mathbf{x}_n \in \mathbb{R}^d$ ($d = 3$ in this paper) and point properties are $\mathbf{y}_n \in \mathbb{R}^c$, the regression model estimation is $f(\mathbf{x}) = E[\mathbf{y}|\mathbf{X} = \mathbf{x}]$.

Gaussian process assumes data are sampled from multivariate Gaussian distribution, i.e.,

$$\begin{bmatrix} \mathbf{y} \\ \mathbf{y}_* \end{bmatrix} \sim \mathcal{N}(\mathbf{0}, \begin{bmatrix} \mathbf{K}(\mathbf{X}, \mathbf{X}) & \mathbf{K}(\mathbf{X}, \mathbf{X}_*) \\ \mathbf{K}(\mathbf{X}_*, \mathbf{X}) & \mathbf{K}(\mathbf{X}_*, \mathbf{X}_*) \end{bmatrix}). \quad (1)$$

With the derivative in [35], we yield

$$\mathbf{y}_*|\mathbf{X}, \mathbf{y}, \mathbf{X}_* \sim \mathcal{N}(\mathbf{K}_*, \mathbf{K}^{-1} \mathbf{y}, \mathbf{K}_{*,*} - \mathbf{K}_*, \mathbf{K}^{-1} \mathbf{K}_*). \quad (2)$$

When an additional Gaussian error is appended, $\mathbf{y} = f(\mathbf{x}) + \epsilon$, the covariance of \mathbf{X} is rewritten as $\mathbf{K} + \delta_n^2 \mathbf{I}$. The regression result is usually considering the mean

$$\mathbf{y}_* = \mathbf{K}_*, (\mathbf{K} + \delta_n^2 \mathbf{I})^{-1} \mathbf{y}. \quad (3)$$

Which well-reveals the challenge to use Gaussian process regression directly in large-scale reconstructions, as $O(n^3)$ time complexity is unaffordable. In addition, such a formula (Eq. (3)) is not usable as the input large point cloud data is required to be maintained for the \mathbf{K}_* computation.

To cope with the high-complexity and to avoid the maintenance of the point cloud, we propose to decouple the GPR to approach the low-dimensional latent vector for local regions. The decoupling requires an approximation of the kernel function

$$\mathbf{K}(\mathbf{X}, \mathbf{X}_*) \approx f_{\text{posi}}(\mathbf{X})^T f_{\text{posi}}(\mathbf{X}_*) \quad (4)$$

where $f_{\text{posi}} : \mathbb{R}^3 \rightarrow \mathbb{R}^l$. We name f_{posi} positional encoding function to be coherent to Neural Implicit Maps model Di-Fusion [11]. Thus, Eq. (3) is rewritten as

$$\mathbf{y}_* = f_{\text{posi}}(\mathbf{X}_*)^T f_{\text{enc}}(\mathbf{X}, \mathbf{y}) \quad (5)$$

where the content encoder function is

$$f_{\text{enc}}(\mathbf{X}, \mathbf{y}) = f_{\text{posi}}(\mathbf{X})(f_{\text{posi}}(\mathbf{X})^T f_{\text{posi}}(\mathbf{X}) + \delta_n^2 \mathbf{I})^{-1} \mathbf{y} \in \mathbb{R}^{l \times c}. \quad (6)$$

We denote the encoded feature as $\mathbf{F}_{(\mathbf{X}, \mathbf{y})} = f_{\text{enc}}(\mathbf{X}, \mathbf{y}) \in \mathbb{R}^{l \times c}$. This is the basis for latent map construction in following universal continuous mapping model (Section IV). To be more specific, for geometry encoding we have $l = 20$ and $c = 1$, thus, the feature is a 20-dimensional vector. For color encoding we yield $l = 20$ and $c = 3$.

Correspondingly, the decoding value for inferencing point \mathbf{x}_* is

$$f_{\text{dec}}(\mathbf{x}_*, F_{(\mathbf{X}, \mathbf{y})}) = f_{\text{posi}}(\mathbf{x}_*)^T F_{(\mathbf{X}, \mathbf{y})}. \quad (7)$$

Thus, a signed distance field or surface property field is approached.

In the following, we derive the approximation function.

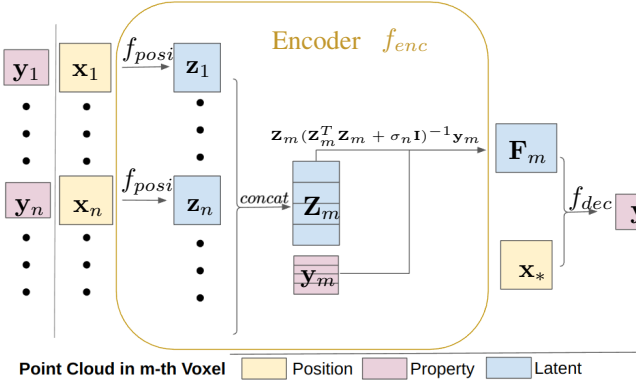


Fig. 3. Interpreting formula with a graph that is coherent to the Encoder-decoder structure in Neural Implicit Maps [11].

B. Position Encoding with Approximated Kernel Function

Considering our mapping requires encoding of local geometry & property, the encoding function merely touch points in a limited region ($[-.5, .5]^3$ in our case).

As we introduced in related works, the Nyström methods, different from the RFFs, are more accurate because it is dependent to the given points. This property well match to our application.

Nyström method for kernel approximation starts with eigenfunctions according to Mercer's theorem:

$$k(\mathbf{x}_1, \mathbf{x}_2) = \sum_{i \geq 1} q_i \psi_i(\mathbf{x}_1)^T \psi_i(\mathbf{x}_2) \quad (8)$$

where ψ_i and $q_i \geq 0$ are eigenfunctions and eigenvalues of kernel $k(\mathbf{x}_1, \mathbf{x}_2)$ with respect to probability measure q .

Given third set of anchor samples $\hat{\mathbf{X}} = \{\hat{\mathbf{x}}_1, \dots, \hat{\mathbf{x}}_N\}$, we eigen-decompose matrix $\mathbf{K}(\hat{\mathbf{X}}, \hat{\mathbf{X}})$ for its eigenpairs $\{(\lambda_i, \mathbf{u}_i)\}_{i \in \{1, \dots, l\}}$ with rank l .

Then Nyström method produces

$$\psi_i(\mathbf{x}) = \sum_n k(\mathbf{x}, \hat{\mathbf{x}}_n) \mathbf{u}_{i,n}, \forall i > 1. \quad (9)$$

For simplicity, we rewrite eigenfunction as

$$\psi_i(\mathbf{x}) = \mathbf{K}(\mathbf{x}, \hat{\mathbf{X}}) \mathbf{u}_i. \quad (10)$$

And correspondingly eigenvalue $q_i = \frac{1}{\lambda_i}$.

To clarify the presentation, we notate $\mathbf{q} = [q_1, \dots, q_l]$ and $\Psi = [\psi_1, \dots, \psi_l]^T$ from Eq. (8) where $\Psi: \mathbb{R}^3 \rightarrow \mathbb{R}^l$.

Make the formula further coherent to Eq. (4), we set

$$f_{posi}(\mathbf{x}) = \text{diag}(\sqrt{\mathbf{q}}) \Psi(\mathbf{x}) \quad (11)$$

where diag produce diagonal matrix. f_{posi} above is the position encoder in the Eq. (6).

In this paper, we utilize Matérn kernel¹:

$$k(\mathbf{x}_i, \mathbf{x}_j) = \sigma^2 \frac{2^{1-\nu}}{\Gamma(\nu)} \left(\sqrt{2\nu} \frac{\text{dist}(\mathbf{x}_i, \mathbf{x}_j)}{\rho} \right) K_\nu \left(\sqrt{2\nu} \frac{\text{dist}(\mathbf{x}_i, \mathbf{x}_j)}{\rho} \right) \quad (12)$$

where Γ is gamma function, K_ν is the modified Bessel function of the second kind, dist denotes the euclidean distance,

¹https://en.wikipedia.org/wiki/Matérn_covariance_function

σ and ρ are kernel's hyper-parameters. We utilize half integer $\nu = 3 + \frac{1}{2}$ and thus the specific function is

$$k(d) = \sigma^2 \left(1 + \frac{\sqrt{7}d}{\rho} + \frac{2}{5} \left(\frac{\sqrt{7}d}{\rho} \right)^2 + \frac{1}{15} \left(\frac{\sqrt{7}d}{\rho} \right)^3 \right) \exp \left(-\frac{\sqrt{7}d}{\rho} \right) \quad (13)$$

where $d = \text{dist}(\mathbf{x}_i, \mathbf{x}_j)$ for short. To approximate above kernel, we first uniformly sample 256 points $\hat{\mathbf{X}}$ in $[-5, 5]^3$ cube to compute kernel $\mathbf{K}_a = \mathbf{K}(\hat{\mathbf{X}}, \hat{\mathbf{X}})$. Then eigendecomposition is applied to this kernel, $\mathbf{K}_a = \mathbf{U} \Lambda \mathbf{U}^T$.

Note that, the encoded feature dimension l used in Section III-A is depend on the \mathbf{U} . Which further determines the map size in the next section (Section IV). There is a trade-off between the approximation and map size.

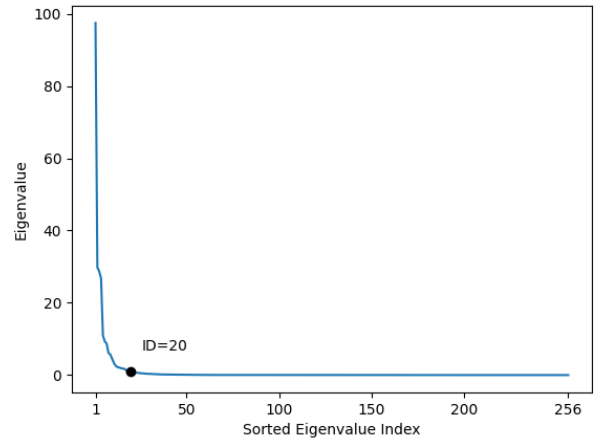


Fig. 4. Sorted eigenvalues for $\mathbf{K}_{a,a}$'s eigendecomposition.

We plot the eigenvalue from Λ in Fig. 4 and find the matrix is mainly affect by the few pairs with large eigenvalues. Most of the eigenvalues are lower than 1. We thus choose $l = 20$ which is around 0.8 in that plot to approximate the kernel while maintain a small feature dimension.

Note that, we only sample and decompose once. Then encoding-decoding in Fig. 3 merely need to load and reuse the parameters for the f_{posi} , f_{enc} and f_{dec} . Related works requires pretrain on large dataset of objects [11], [16] or indoor scenes [14]. But for our model **no training is needed**.

IV. UNIVERSAL CONTINUOUS MAPPING

The previous Section III proposes universal encoding model for various data. Taking that function as a basis, in this section, our Universal Continuous Mapping produces a map of latents to implicitly represent the scene. We name such scene representation **Latent Implicit Maps (LIM)**. Which supports surface, surface properties, and high-dimensional surface features.

The inheritance graph is plotted in Fig. 5. We design a BaseMap for operating the voxel structure (Section IV-A), dynamically allocating space and fusing maps (Section IV-E). The derived SurfaceMap (Section IV-B) and PropertyMap (Section IV-C) process specific data and operate for the specific application. The LatentMap (Section IV-D) is derived

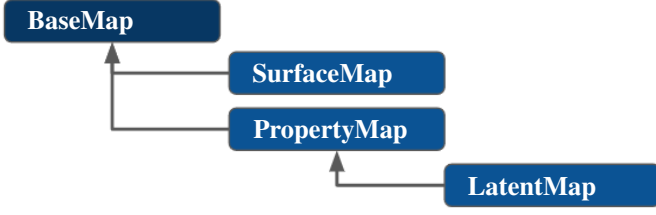


Fig. 5. Inheritance graph for the class of Latent Implicit Maps (LIM).

from PropertyMap. The main difference is that the PropertyMap mainly operates low dimensional properties, such as color ($c = 3$) or infrared ($c = 1$) data, etc. While the LatentMap operates much higher dimensional feature, such as CLIP embeddings [18] ($c = 768$), for different application purposes.

A. Map Representation

We follow Neural Implicit Maps ([11], [12], [16]) to use uniform-spaced voxels to sparsely represent the scene. The scene is $\mathbf{V} = \{\mathbf{v}_m = (\mathbf{c}_m, \mathbf{F}_m, w_m)\}$. m is the voxel index. \mathbf{v}_m denotes the contents of that voxel which are $\mathbf{c}_m \in \mathbb{R}^3$, $\mathbf{F}_m \in \mathbb{R}^{l \times c}$ and $w_m \in \mathbb{N}$ respectively representing the voxel center, voxel latent feature and observed points count.

With a sequence of incremental frames as input, our model constructs local LIMs (Section IV-B, Section IV-C, Section IV-D) and fuses (Section IV-E) into a global LIM. Then the resulting explicit map is inferred from the global LIM.

B. Surface Mapping

Because the input point cloud \mathbf{X} is on zero-level of the surface, it is not adequate to recover a 3D field of scene, $f_{SDF} : \mathbb{R}^3 \rightarrow \mathbb{R}$. Thus, we exploit the idea of Gaussian Process Implicit Surfaces (GPIS) [4]–[7] to feed derivatives to kernel or to additionally sample non zero-level points. Both, derivative-based and sample-based GPISs use normal information. Thus, we first pre-process \mathbf{X} to obtain normals \mathbf{S} .

1) *Using Derivatives based GPIS*: From [4], derivatives of a GP are also Gaussian. So the covariance between data and derivatives is the differentiation of the covariance function [36]:

$$\begin{aligned} \text{cov}\left(\frac{f_{SDF}(\mathbf{x})}{\partial x_i}, f_{SDF}(\mathbf{x}')\right) &= \frac{\partial k(\mathbf{x}, \mathbf{x}')}{\partial x_i} \\ &= \frac{\partial}{\partial x_i} [f_{posi}(\mathbf{x})]^T f_{posi}(\mathbf{x}'). \end{aligned} \quad (14)$$

Additionally,

$$\begin{aligned} \text{cov}\left(\frac{f_{SDF}(\mathbf{x})}{\partial x_i}, \frac{f_{SDF}(\mathbf{x}')}{\partial x_j}\right) &= \frac{\partial^2 k(\mathbf{x}, \mathbf{x}')}{\partial x_i \partial x_j} \\ &= \frac{\partial}{\partial x_i} [f_{posi}(\mathbf{x})]^T \frac{\partial}{\partial x_j} [f_{posi}(\mathbf{x}')]. \end{aligned} \quad (15)$$

So given points $\{\mathbf{x}_n\}_{n=1}^N$ with normals $\{\mathbf{s}_n\}_{n=1}^N$ and field values $\{\mathbf{y}_n = 0\}_{n=1}^N$, the positional encoding function for derivatives is $f_{posi,deri}(\mathbf{x}, i) = \frac{\partial}{\partial x_i} [f_{posi}(\mathbf{x})]$. Its corresponding field value is the normal value s_i on the axis i . Then,

$$\begin{aligned} f_{posi,gpis}(\mathbf{X}) &= \\ [f_{posi}(\mathbf{X}), f_{posi,deri}(\mathbf{x}, 1), f_{posi,deri}(\mathbf{x}, 2), f_{posi,deri}(\mathbf{x}, 3)] \end{aligned} \quad (16)$$

with regression values $\mathbf{y}_{gpis} = [\mathbf{0}, \mathbf{s}_{\cdot,1}, \mathbf{s}_{\cdot,2}, \mathbf{s}_{\cdot,3}]^T$, where $\mathbf{0} = \text{zeros}(1, N)$, $\mathbf{s}_{\cdot,i} = [s_{1,i}, \dots, s_{N,i}]$.

Therefore the local geometric encoding function is

$$\begin{aligned} f_{enc,GPIS}(\mathbf{X}, \mathbf{y}, \mathbf{S}) &= \\ f_{posi,gpis}(\mathbf{X}) (f_{posi,gpis}(\mathbf{X})^T f_{posi,gpis}(\mathbf{X}) + \sigma_n^2 \mathbf{I})^{-1} \mathbf{y}_{gpis}. \end{aligned} \quad (17)$$

By introducing derivation into kernels, the matrix size is enlarged 15-times, while the encoded feature is still of low dimension l : $F_{\mathbf{X}, \mathbf{y}, \mathbf{S}} = f_{enc,GPIS}(\mathbf{X}, \mathbf{y}, \mathbf{S}) \in \mathbb{R}^l$.

For inference with the points \mathbf{x}_* , predictions are consistent to Eq. (7), $y_* = f_{posi}(\mathbf{x}_*)^T F_{\mathbf{X}, \mathbf{y}, \mathbf{S}}$.

2) *Using Sample based GPIS*: Sample-based GPIS are mostly used in GPIS researches. This is because such method does not compute Jacobians and the kernel size can be small. This highly-reduces the processing cost both on time and memory. Given points $\{\mathbf{x}_n\}_{n=1}^N$ with normals $\{\mathbf{s}_n\}_{n=1}^N$ and field value $\{\mathbf{y}_n = 0\}_{n=1}^N$, sample-based GPIS extends the dataset by sample points along the normal direction. Corresponding field values are the signed distance as the sampled points walk along the normal. Afterwards, with the extended points and distances $\mathbf{X}_{ext}, \mathbf{y}_{ext}$, Eq. (6) is applied. The inference of such model is the same as derivative-based GPIS Section IV-B1.

For each frame, points are distributed to its corresponding voxel. Then we encode the local geometry in voxel using Section IV-B1 or Section IV-B2 to obtain $\mathbf{v} = (\mathbf{c}, \mathbf{F}, w)$ with $\mathbf{F} \in \mathbb{R}^l$ the geometric latent vector. Then local LIMs are fused to a global LIM following Section IV-E.

To achieve a surface result for visualization, we construct the Signed Distance Field from global LIM by inferring on sample points. The sample points are from a grid in each voxel with a certain resolution. By applying the MarchingCube algorithm on SDF, a surface mesh is obtained.

C. Surface Property Fields

The previous surface mapping (Section IV-B) can be considered as a special case of this Surface Property Mapping. But the two mappings actually do not handling in the same space. More precisely for implementation, we do not derive the SurfaceMap class from PropertyMap. Instead, as shown in Fig. 5, we further introduce a BaseMap to perform the common operations and let them operate specifically on local map construction and visualization, e.g., meshing and coloring.

We introduce the more general mapping of surface properties. Since the points are all on zero-level in signed distance fields, the PropertyMap naturally handles in a subspace of \mathbb{R}^3 ,

the surface \mathcal{S} . A surface property in this paper could be any properties for each point, such as color, infrared, and etc. They only differ on \mathbf{y} in Fig. 3 with dimension c .

We set the most widely used data color as an example. Given an observed colored point cloud $\{(\mathbf{x}_n, \mathbf{c}_n) | n = 0 \dots N\}$ as input, where \mathbf{c}_n denote the RGB. Its surface field properties values are $\{\mathbf{y}_n = \mathbf{c}_n\}_{n=1}^N$. We aggregate the values in two $N \times 3$ matrices \mathbf{X} and \mathbf{C} . So encoded feature for this point cloud is

$$\mathbf{F}_{color} = f_{posi}(\mathbf{X})(f_{posi}(\mathbf{X})^T f_{posi}(\mathbf{X}) + \delta_n^2 \mathbf{I})^{-1} \mathbf{C}, \quad (18)$$

where $\mathbf{F}_{color} \in \mathbb{R}^{l \times 3}$.

Since we use $l = 20$ in the approximation function for experiments, the color feature are small. The color map only stores 20×3 float in each voxel for a continuous color field. Note that, our model does not need any training. It can be directly applied to different types of data. For the inference, because the field is on the surface space, we sample points \mathbf{x}_* in arbitrary resolution, from the given know mesh or surface construction of a previous surface mapping (Section IV-B). Following Eq. (7), the inference points \mathbf{x}_* are positional-encoded and directly multiplied with color feature $\mathbf{F}_{color,m}$ in the corresponding voxel m to obtain its value $\mathbf{c}_* = f_{dec}(\mathbf{x}_*, \mathbf{F}_{color,m})$.

D. Surface Feature Fields

Surface Feature Fields are considered as an extensive use of previous Surface Property Fields (Section IV-C). Here we extend the surface properties scope to include features. This extension further demonstrates the capability of our mapping model as it is directly used without any training.

Given an embedding function $\phi : \mathbb{R}^{N \times 3} \rightarrow \mathbb{R}^{N \times c}$ to process the data \mathbf{X} , we approach the feature of each point as surface properties $\{\mathbf{y}_n = \phi(\mathbf{X})_{\mathbf{x}_n} \in \mathbb{R}^{l \times c}\}_{n=1}^N$.

Following the encoding and fusion as Section IV-C and Section IV-E, we construct latent implicit maps for the surface feature fields. Thus, arbitrary resolutional maps of feature are extracted with $f_{dec}(\cdot, \mathbf{F})$.

We provide one application in Section V-C: Open Vocabulary Scene Understanding. Our model constructs a CLIP space feature field on the surface. And is therefore able to answer a text input. The differences compared to Surface Property Fields are demonstrated in Fig. 6. In (c), a CLIP text encoder f_{text} is appended to encode the text command \mathbf{u} to the CLIP feature \mathbf{U} . Considering the left branch produces a surface field for CLIP embeddings, our model is capable to find the wanted region by computing the similarity between features.

E. Map Fusion

We follow Neural Implicit Maps [11] to update the LIM in a voxel-to-voxel manner:

$$\mathbf{F}_m \leftarrow \frac{\mathbf{F}_m w_m + \mathbf{F}'_m w'_m}{w_m + w'_m}, w_m \leftarrow w_m + w'_m, \quad (19)$$

where $\mathbf{v}_m = (\mathbf{c}_m, \mathbf{F}_m, w_m)$ and $\mathbf{v}'_m = (\mathbf{c}'_m, \mathbf{F}'_m, w'_m)$ are the voxel m from global and local LIMs respectively.

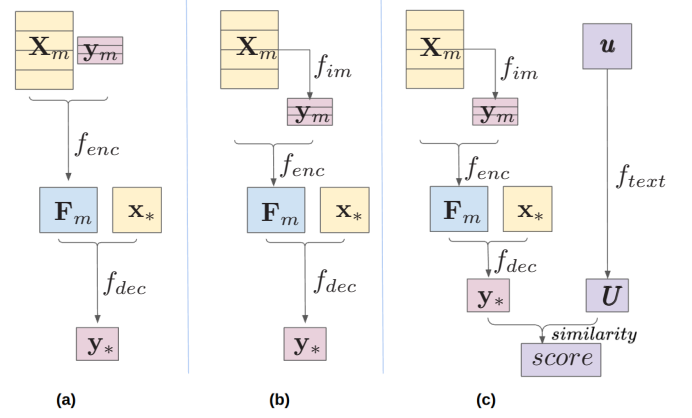


Fig. 6. Encoding-decoding diagram in different applications. (a) fold applications directly obtain point properties (\mathbf{y}_m) from sensor. (b) fold applications achieves point properties with (style, saliency and etc.) function ϕ_{im} . (c) fold applications use feature as \mathbf{y}_m to build a LIM for a (CLIP) feature field. Then a text command is used for extracting the semantic information.

V. APPLICATIONS

To demonstrate the wide range of usages of our model, we implement a series of applications:

- 1) Incremental surface & color reconstruction
- 2) 3D saliency detection
- 3) Open vocabulary scene understanding
- 4) Surface infrared field
- 5) 3D style transfer

Originating from our motivation in inspection and service robotics, we implement 1) Incremental surface & color reconstruction for visualization of robot surroundings. For robot exploration, we implement 2) 3D saliency detection to indicate the salient regions in maps. For recovering object-level semantic information in environments, we implement 3) open vocabulary scene understanding to yield the regions containing the objects.. Furthermore, to demonstrate the flexibility, we implement 4) surface infrared fields and 5) 3D style transfer for artistic purposes.

In Fig. 6, we classify those 3 applications into 3 categories: (a) directly obtaining the properties from sensor observation, such as application 1) and 4). (b) processing on sensor data and predict properties, such as application 2), 5). (c) extending (b) to operating beyond latent features, such as application 3).

Application 1) and 4) are in the first one category. Thus, we mainly describe 1) incremental surface & color reconstruction (Section V-A), while for 4) we can easily exchange color with infrared. For the second with 2) and 5) in Section V-B, we mainly describe the usage of fabricated properties. As the mapping part is redundant to previous category, it will not be detailed. The third category is the application 3) that maps a LIM for high dimensional latent fields. We demonstrate that this application provides a flexible inference in Section V-C.

A. Application: Incremental Reconstruction

In this section, we build an incremental 3D reconstruction application with RGBD sequences. Since RGBD sequences

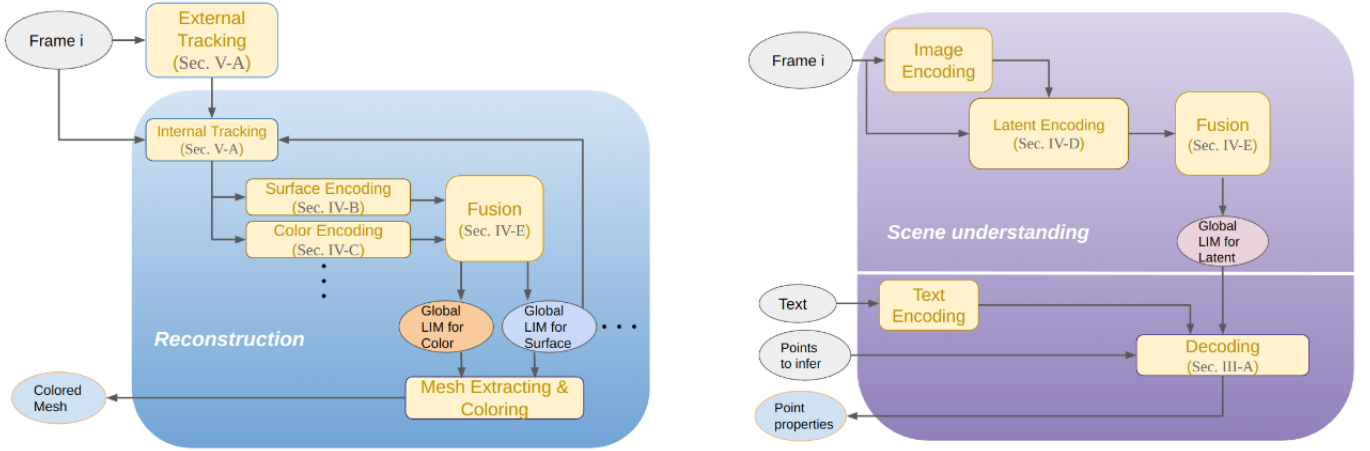


Fig. 7. Reconstruction and scene understanding applications pipeline. On the left incremental reconstruction application, external tracking runs in parallel to reconstruction to provide coarse poses. While reconstructing, internal tracking refines the pose estimation to have better surface fit. “...” means that we can add more other properties from Section V-A2 and Section V-B into this pipeline. On the right scene understanding application, we assume the pose of the frame is pre-known. The upper part of the white line is the fusing of LIM for the feature field. The lower part infers specific semantic information by input text command.

provide point positions and color values, the application constructs two kinds of LIMs: one for surface (Section IV-B), and one for color (Section IV-C).

The pipeline is shown in Fig. 7. When a RGBD frame i is fed into the framework, it is firstly converted to a colored point cloud ($\mathbf{X} \in \mathbb{R}^{N \times 3}$, $\mathbf{Q} \in \mathbb{R}^{N \times 3}$). Then, tracking module takes (\mathbf{X}, \mathbf{Q}) to compute the current pose \mathbf{T} . Afterwards we feed transformed point cloud $\mathbf{X}\mathbf{T}^T$ into surface mapping (Section IV-B), colored point cloud $(\mathbf{X}\mathbf{T}^T, \mathbf{Q})$ into surface color mapping (Section IV-C) to obtain the local LIMs. With Eq. (19), we fuse local LIM to global LIM voxel-to-voxel.

For visualization, we first sample the grid in each voxel and inference with the global surface LIM to achieve the SDF. The MarchingCube algorithm is applied to extract the mesh.

With the surface reconstructed, we are able to sample points in an arbitrary resolution from it and inference with global color LIM to reconstruct the surface color.

1) *Tracking*: From [14], we find that the current implicit scene representation based tracking models, i.e., iMAP, DI-Fusion and NICE-SLAM, still have a performance gap to state-of-the-art tracking approaches like BAD-SLAM and ORB-SLAM2. Thus, instead of following the neural implicit models to track with frame-to-model or ray-tracing based optimization, we run ORB-SLAM2 in the other thread to provide the pose prior.

To note that, the SLAM model is designed for localization which cares less on reconstruction. This means directly utilizing ORB-SLAM2 provides coarse surface construction. We further use colored point cloud registration (CPCR) [37] as the tracking refiner for better surface and color fitness. This is tested much more robust than more recent tracking algorithms in fusion models. ORB-SLAM2 runs independently over all frames. Every few frames, CPCR track one initially posed colored point cloud to compute the odometry in local window. Mapping is applied afterwards.

2) *Other types of datas*: Application 4) uses a point cloud with infrared, which is simply replacing the color

with infrared. LIM feature dimension is also correspondingly reduced. For all other kind of point cloud properties, this application is easily adapted.

B. Application: 2D-to-3D Transfer

Applications like 2) and 4) work easily alongside application 1): incremental reconstruction (Section V-A) by feeding the fabricated result together with the point cloud. For example, given RGB-D frames, we detect saliency or transfer image styles for a fabricated X image. Here X denotes saliency, style, and etc. Then by unprojecting it together with depth, the fabricated value is assigned to points for points pairs $(\mathbf{X}, \mathbf{C}_X)$.

Similar to Fig. 7 the reconstruction pipeline, with encoding (Section III-A) and fusion (Eq. (19)), a global LIM for the fabricated properties X is constructed. Which is also a surface X fields for later inference. It is also possible to similarly transfer a 2D semantic image to 3D. But it is not affordable as different types of semantic information may requires a remapping on the same data. Therefore in the following, we demonstrate construction of a surface feature field for the scene understanding application that uses one pass of mapping to meet various needs.

C. Application: Open Vocabulary Scene Understanding

This application follows OpenScene [38], a learning approach that predicts dense features for 3D scene points. Where the features are co-embedded with text and image pixels in CLIP feature space. Inspired by this, we designed the mapping for surface feature fields (Section IV-D). The difference comparing to surface property fields is shown in Fig. 6. ϕ is taken from pretrained OpenSeg [18]. The voxel latent \mathbf{F}_m is encoded from points and points \mathbf{X}_m features \mathbf{y}_m . During inferencing, given open vocabulary text input \mathbf{u} and position input \mathbf{x}_* , we obtain the CLIP space features. By computing

similarity, the point property is determined. Pipeline of this application is shown in Fig. 7.

In this application, image encoding function f_{im} and text encoding function f_{text} are taken from pre-trained model. While f_{enc} and f_{dec} in our Uni-Fusion are actually deterministic functions. With those functions, our model construct a continues field for the CLIP feature on surface.

An highly-interesting and similar work to Uni-Fusion scene understanding application is VLMaps [39]. This work produces a 2D map while our model produces a surface CLIP feature field in 3D space.

VI. EXPERIMENTS

In this section, we demonstrate the wide-range of usages and high capabilities of Uni-Fusion on various applications. First, we evaluate Uni-Fusion on application 1) Incremental Surface and Color Reconstruction with respect to the SOTAs. Considering that the applications 2) and 5) are a novel topic, we cannot find related benchmarks for comparison. Thus, we demonstrate the performance on exist results. Afterwards, application 3) is implemented and compared to the SOTA zero-shot semantic segmentation models. Finally, for application 4) as infrared data is not widely used, we capture our own dataset containing infrared and demonstrate all applications on it.

A. Implementation Details

In the experiments, we use our sample-based GPIS for local geometry encoding. For each point, 2 points along normal direction are sampled (one positive, one negative) with distance $d = 0.1$ in the local voxel's normalized space. Comparing to derivative-based GPIS, our sample based GPIS is more efficient in both space and time. For the encoder, we use 256 anchor points that are randomly sampled from $[-0.5, 0.5]^3$. The first 20 eigen-pairs are utilized, which yield the feature dimension 20. The model choosing will be discussed in ablation study.

Different maps of latents use different granularity. For surface LIM, we use voxel-size 5cm. For color which requires later comparison to NeRF, we use voxel-size 2cm. For other property LIM and feature LIM, we use voxel-size 10cm.

For smoothness of reconstruction, the encoded voxel is overlapped. This means it uses the double-size to ensure a half space overlap with each neighbor. Then during meshing, SDF is fetched from the overlapped voxel. While for the remaining properties, we only sample from its own voxel part.

The implementation runs on a computer with AMD Ryzen 9 5950X 16-core CPU and a Nvidia Geforce RTX 3090 GPU (24 GB).

B. Datasets

We evaluate incremental reconstruction on the ScanNet dataset [40], TUM RGB-D dataset [41], and Replica dataset [13]. Using MSG-Net [42]'s material set, we transfer styles to the 3D canvas. For Open Vocabulary Scene Understanding, we evaluate on ScanNet segmentation data [43] and S3DIS dataset [44].

1) *ScanNet* [40]: ScanNet is a densely annotated RGB-D video dataset. It is captured with the structure sensor [45] and contains 1513 scenes for training and validation. For each scene, both images and a 3D mesh is provided, together with their 2D, 3D semantic annotations.

ScanNet provide 312 scenes for validation, which contains a wide range of various room structures. It has now been widely used in the thorough evaluation of the performance of reconstruction and semantic segmentation.

2) *TUM RGB-D* [41]: TUM RGB-D is a benchmark to mainly evaluate the performance of tracking. It is captured with Microsoft Kinect sensor together with ground-truth trajectory from the sensor.

3) *Replica* [13]: Replica dataset is referred to iMAP's pre-processed dataset [13]. It is a synthetic rendered RGB-D dataset from given 3D models. The advantage to include this dataset is that Replica does not have motion blur. Which is better to evaluate the capability of algorithms on reconstructing surface color.

4) *MSG-Net Style* [42]: MSG-Net provide material images for transferring the styles. We select 21style fold for demonstration. Those images are given in Fig. 13 together with our result.

5) *ScanNet Point Cloud Segmentation Data* [43]: For point cloud semantic segmentation benchmarking, PointNet++ [43] pre-processes the original ScanNet [40] and generates sub-sampled point clouds and corresponding annotations for each scene.

6) *S3DIS* [44] and *2D-3D-S* [46]: S3DIS is a semantic segmentation dataset for 3D point clouds. Which is also a subset of the 2D-3D-S dataset. The 2D-3D-S dataset is a multi-modalities dataset containing 2D, 2.5D and 3D domains. This dataset is densely annotated with semantic labels.

Note that 2D-3D-S's 2D captures is not a RGB-D video as ScanNet. 2D-3D-S's images only have small overlap. So it is merely for semantic segmentation and not capable for incremental reconstruction application.

C. Baselines

For online surface mapping evaluation, we choose TSDF Fusion [8], iMAP [13], SOTA DI-Fusion [11] and BNV-Fusion [16] as four baselines methods.

For the color field, we choose TSDF Fusion [8], σ -Fusion [47], iMAP [13], NICE-SLAM [14] and even recent hot Neural Radiance Fields model NeRF-SLAM [17] as five baselines. Even though it is not fair to include NeRF in comparison, we show in following experiment that Uni-Fusion significantly reduce the gap.

For Scene Understanding application, we evaluate generalized zero-shot point cloud semantic segmentation with ZSLPC [48], DeVise [49] and SOTA 3DGenZ [50] for comparison.

D. Metrics

For incremental reconstruction, we evaluate the geometric reconstruction using **Accuracy**, **Completeness**, and **F1 score**. We follow BNV-Fusion [16] to uniformly sample

TABLE I

COMPARISON TO SCANNet [40]. OUR METHOD GENERALIZES BETTER TO VARIOUS SCENES. * INDICATES THE RESULT FROM OUR RUNS OF THE OFFICIAL BNV-FUSION CODE.

Method	Pre-Train with extra dataset	Train with sequences	Real-time	Accuracy (%) \uparrow	Completeness (%) \uparrow	F1 score \uparrow
TSDf Fusion [51]	None	None	✓	73.83	85.85	78.84
iMAP [13]	None	Online train		68.96	82.12	74.96
DI-Fusion [11]	Object Pretrain	None	✓	66.34	79.65	72.97
BNV-Fusion [16]	Object Pretrain	Post Optimization		74.90	88.12	80.56
BNV-Fusion* [16]	Object Pretrain	Post Optimization		73.42	81.75	77.18
Uni-Fusion (Ours)	None	None	✓	80.43	84.91	82.44

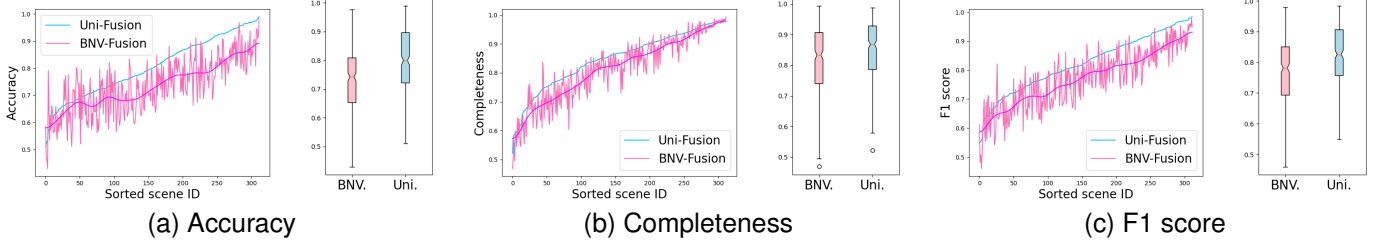


Fig. 8. Quantitative comparison on 312 scenes of the ScanNet validation set. We demonstrate the performance of SOTA BNV-Fusion and our Uni-Fusion. We sort our evaluation value and reordered all of the scores. The zigzag pink is the BNV-Fusion result; we also plot a deep-pink smoothed curve for better visualization.

100,000 points from reconstruction and ground-truth mesh respectively. Then **Accuracy (Completeness)** measures the percentage of reconstruction-to-ground-truth (ground-truth-to-reconstruction) distances that are lower than 2.5cm threshold. **F1 score** is the harmonic mean of accuracy and completeness. For tracking performance, we use **ATE RMSE**.

Then for evaluation of color reconstruction, we follow SOTA on this topic, the NeRF to render both depth and RGB images to compare the image level **Depth L1** and **RGB PSNR**.

Afterwards, for comparing scene understanding, we follow zero-shot point cloud semantic segmentation SOTA 3DGenZ to evaluate the **Intersection-of-Union (IoU)** and **Accuracy**.

E. Reconstruction Results

For evaluation, we first use the ScanNet validation set with 312 sequences to thoroughly test the geometric reconstruction on a large variant of scenes. Then, we use TUM RGB-D to compare our modified tracking model with related works. Because this part is not the main contribution, we give a rough overview of the tracking results. To fairly evaluate the color reconstruction, we use the high quality rendered Replica dataset to compare with related works, including NeRF.

1) *Evaluation on ScanNet Dataset [40]:* We use the 312 diversified scenes from the ScanNet validation set to evaluate the performance of surface reconstruction. We follow the pure mapping SOTA BNV-Fusion to take every 10th posed frame as input. Without using any learning (in contrast iMAP, DI-Fusion, and BNV-Fusion do) or any post optimization (as BNV-Fusion does), our Uni-Fusion is capable to achieve precise continuous mapping performance.

As shown in Table I, our Uni-Fusion achieves +6 **higher accuracy** than the incremental surface reconstruction SOTA BNV-Fusion. Our model does not exceed on completeness

comparing to BNV-Fusion that support completion in post-optimization. Though, Uni-Fusion’s completion is still much higher than one other optimization based model iMAP. Overall, our Uni-Fusion model achieves higher F1-scores that quantifies the overall quality.

Please note that, SOTA BNV-Fusion is not real-time capable, since it requires post optimization of all fed frames. Without the post-optimization, the real-time model Di-Fusion shows much worse results. However, our **real-time** model **Uni-Fusion** is able to achieves **much better** reconstruction quality than these approaches even without post-optimization.

We additionally run BNV-Fusion’s official implementation (emphasized with *) on the 312 videos of ScanNet and do a post element-wise comparison in Section VI-E. Our result is the **light blue** curve, BNV-Fusion’s result is colored with **pink**. Scene index is sorted corresponding to the score value of Uni-Fusion. For better visualization, we smooth BNV-Fusion’s curve and plot it with dark pink. It is obvious that the score of Uni-Fusion is overall higher than BNV-Fusion’s. Moreover, we use box-plot to conclude the statistics besides the curve plot. Uni-Fusion’s scores are distributed in a higher region. For completeness which is less obvious better, Uni-Fusion’s box is smaller while in a relative higher position. This means that Uni-Fusion has more stable completeness result while BNV-Fusion is more likely to get low completeness in some cases.

To summarize, our model is almost better on all 312 scenes on all accuracy, completeness and F1-score. Which is also revealed in Table I with BNV-Fusion*, that the BNV-Fusion’s official implementation does not exceed Uni-Fusion on all metrics.

We plot reconstruction on selected scenes from ScanNet in Fig. 9. Both BNV-Fusion and our Uni-Fusion are able to produce high quality reconstruction. We see that BNV-Fusion gives lots of small meshes on walls, which are shown as small

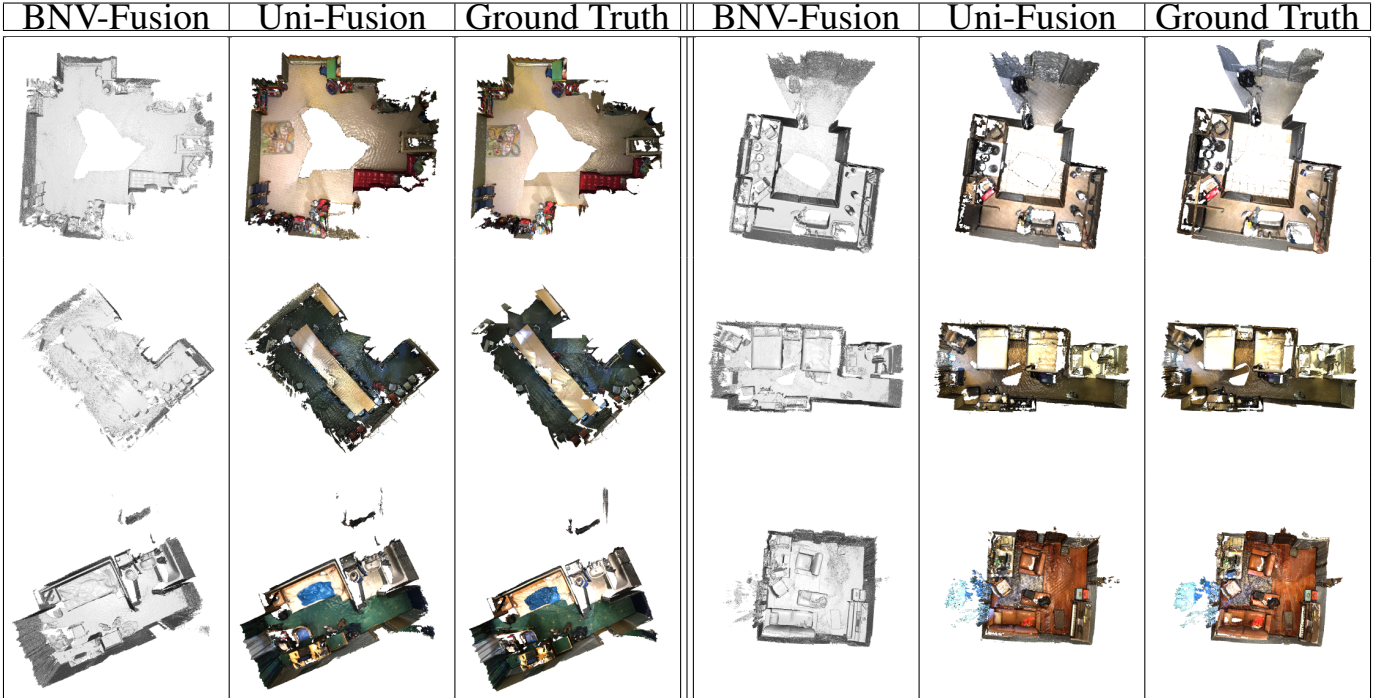


Fig. 9. Surface reconstruction on ScanNet dataset.

TABLE II
TRACKING ON TUM RGB-D [41]. ATE RMSE [cm] (\downarrow) IS USED AS THE EVALUATION METRIC.

	fr1/desk	fr2/xyz	fr3/office
iMAP [13]	4.9	2.0	5.8
iMAP* [13]	7.2	2.1	9.0
DI-Fusion [11]	4.4	2.3	15.6
NICE-SLAM [14]	2.7	1.8	3.0
Ours	1.8	0.5	2.1
BAD-SLAM [52]	1.7	1.1	1.7
Kintinous [53]	3.7	2.9	3.0
ORB-SLAM2 [54]	1.6	0.4	1.0

particles in the reconstruction. We consider it is because BNV-Fusion use very small voxel size (0.02m) to get a high score. This is also revealed by their 247 MB mesh in average, while ours is only 54 Mb in average. Furthermore, our Uni-Fusion’s mesh is more smooth and also provides high-precise color to the mesh which is not available for the Surface SOTA.

2) *Tracking Evaluation on TUM RGB-D Dataset [41]:* In the above test, we compare the performance of pure mapping. While tracking is not the contribution focus in our paper, it is part of the reconstruction model. We follow the novel reconstruction model NICE-SLAM [14] to evaluate the camera tracking on the small-scale TUM RGB-D dataset. Our Uni-Fusion uses a coarse-to-fine strategy for 3D reconstruction tracking. From Table II, it demonstrates overall better ATE RMSE than other implicit representation models.

On the other hand, there also exist high accuracy algorithms from SLAM. By additional using Bundle Adjustment and Loop-closing techniques, their tracking quality is much better than all of the implicit based models.

Even though, our coarse-to-fine strategy firstly ensure not easy to lose track. Secondly, it is more suitable for surface

fitting.

Which further support our test in Replica dataset.

3) *Evaluation on Replica RGB-D Dataset [13]:* In this evaluation, we compare with implicit reconstruction (TSDF-Fusion, σ -Fusion) and latent implicit reconstruction models (iMAP, NICE-SLAM) that support colors. We also add a large-scale NeRF model, NeRF-SLAM in to the table. NeRF is SOTA in view-synthesis task, which is unfair to direct compare with the rest. As the rest model does not even model light directions. We add NeRF in this part to demonstrate that Uni-Fusion strongly reduce the gap. Note that, NeRF-SLAM embeds external tracking model [55] to provide poses while using SOTA NeRF implementation Instance-ngp [56] for NeRF construction.

Uni-Fusion track and follow our previous setting in ScanNet test to take every 10 frames for mapping. NICE-SLAM and NeRF-SLAM produce depth and color by rendering. To obtain result from Uni-Fusion, we cast rays from virtual camera to our result surface mesh for depth image. Then Uni-Fusion infer the cast points in Uni-Fusion’s color LIM for color result.

From Table III, Uni-Fusion demonstrate best Depth L1 on all scenes with an average of **1.47cm depth L1**. Which is **177% boost** comparing to the second best.

Moreover, excluding NeRF, our Uni-Fusion also shows the best performance to model the colors with an average of 28.07dB PSNR.

However, it is strange that NICE-SLAM lost details while in two cases, it shows better PSNR than Uni-Fusion. To highlight the true result, we plot the rendered image in Fig. 10. It is obvious that our Uni-Fusion models the details of painting, carpet and quilt well. While NICE-SLAM just roughly models the average color.

Moreover, from the Fig. 10, our Uni-Fusion’s rendering quality is as precise as NeRF. Please also find the painting,

TABLE III
GEOMETRIC (L1) AND PHOTOMETRIC (PSNR) EVALUATION ON THE REPLICA DATASET [13].

		office-0	office-1	office-2	office-3	office-4	room-0	room-1	room-2	Avg.
<i>Non-continuous mapping method</i>										
TSDF-Fusion [8]	Depth L1 [cm] ↓	14.11	10.50	30.89	28.92	22.83	23.51	20.94	23.34	21.88
	PSNR [dB] ↑	11.16	15.92	4.86	5.68	5.46	3.43	4.51	5.57	7.07
σ-Fusion [47]	Depth L1 [cm] ↓	13.80	10.21	22.27	28.70	22.21	21.92	19.28	22.40	20.10
	PSNR [dB] ↑	11.16	15.92	4.86	5.69	5.46	3.45	4.51	5.57	7.08
<i>Continuous mapping method</i>										
iMAP* [13]	Depth L1 [cm] ↓	6.43	7.41	14.23	8.68	6.80	5.70	4.93	6.94	7.64
	PSNR [dB] ↑	7.39	11.89	8.12	5.62	5.98	5.66	5.31	5.64	6.95
Nice-SLAM [14]	Depth L1 [cm] ↓	1.51	0.93	8.41	10.48	2.43	2.53	3.45	2.93	4.08
	PSNR [dB] ↑	22.44	25.22	22.79	22.94	24.72	29.90	29.12	19.80	24.61
Uni-Fusion (Ours)	Depth L1 [cm] ↓	0.79	0.56	1.59	2.71	1.66	1.94	0.69	1.80	1.47
	PSNR [dB] ↑	33.88	33.31	25.84	26.01	28.14	24.02	26.20	27.17	28.07
<i>Neural radiance field method</i>										
NeRF-SLAM [17]	Depth L1 [cm] ↓	2.49	1.98	9.13	10.58	3.59	2.97	2.63	2.58	4.49
	PSNR [dB] ↑	48.07	53.44	39.30	38.63	39.21	34.90	36.95	40.75	41.40

TABLE IV
DIFFERENCES AMONG DIFFERENT SURFACE & COLOR RECONSTRUCTION MODELS.

Method	Pre-Train with extra dataset	Train with sequences	Real-time	Direct Output	Light direction	Render
TSDF-Fusion	None	None	✓	Discrete TSDF		Ray Rasterization
σ -Fusion	None	None	✓	Discrete TSDF		Ray Rasterization
iMAP	None	Online Train		MLPs		Volumetric Rendering
NICE-SLAM	Pretrain with indoor dataset	Online Train		Neural Implicit Grid		Volumetric Rendering
NeRF-SLAM	None	Train hundred epochs	-	NeRF	✓	Volumetric Rendering
Uni-Fusion	None	None	✓	Latent Implicit Map		Ray Rasterization

carpet and quilt, Uni-Fusion recovered the original appearance well. Please find the **green window** for the emphasized region. Uni-Fusion reproduce the high-quality appearance which is very close to NeRF on qualitative evaluation. But, Uni-Fusion still has a quantitative score gap to the color rendering of NeRF (41.4dB). Though the Uni-Fusion’s rendering result is highly close to NeRF and ground truth. We consider the main reasons are that **1.** Uni-Fusion does not model the light directions to points, which is essential to NeRF. **2.** NeRF optimizes on the rendering image quality by focussing mainly on color while less on depth. It can be revealed by the higher color rendering score with much worse depth rendering than our Uni-Fusion. **3.** our Uni-Fusion does not support hole filling. This directly leads to black holes in our rendered images.

We summarize the differences in Table IV. Similar to TSDF-Fusion and σ -Fusion, our Uni-Fusion is a forward method which, does not need any training, i.e., pre- or online training. Uni-Fusion also produces similar to NICE-SLAM and NeRF-SLAM an implicit map with set of latent that outputs results at arbitrary resolution. However, we differ on the extracting of the signed distance field. Uni-Fusion’s latent feature rule its own region independently. Each query value is directly inferred with the corresponding ruling latent. While NICE-SLAM and NeRF-SLAM use a much denser grid to interpolate query

TABLE V
ABLATION STUDY ON TRACKING.

	fr1/desk	fr2/xyz	fr3/office
External	2.1	0.5	2.5
External+Internal	1.8	0.5	2.1

features. This requires volumetric rendering for inference.

Similar to TSDF-Fusion, σ -Fusion, our Uni-Fusion is also a real-time algorithm. iMAP, NICE-SLAM and NeRF-SLAM run hardly in real-time. NeRF-SLAM is claiming to be real-time, which is questionable as they still need hundreds of epochs training after feeding the data.

Nevertheless, optimization with backpropagation learns pixel-to-pixel well. It is theoretically advanced for a regression-and-fusion strategy. Though Uni-Fusion demonstrates its high capability to model the color, NeRF-like post-optimization would still be a good direction for further improvements of Uni-Fusion.

F. Ablation study

1) *Sample-based or Derivative-based:* We select the surface model with our own captured sequences. All settings are detailed in Section VI-A. As shown in Fig. 11, reconstruction

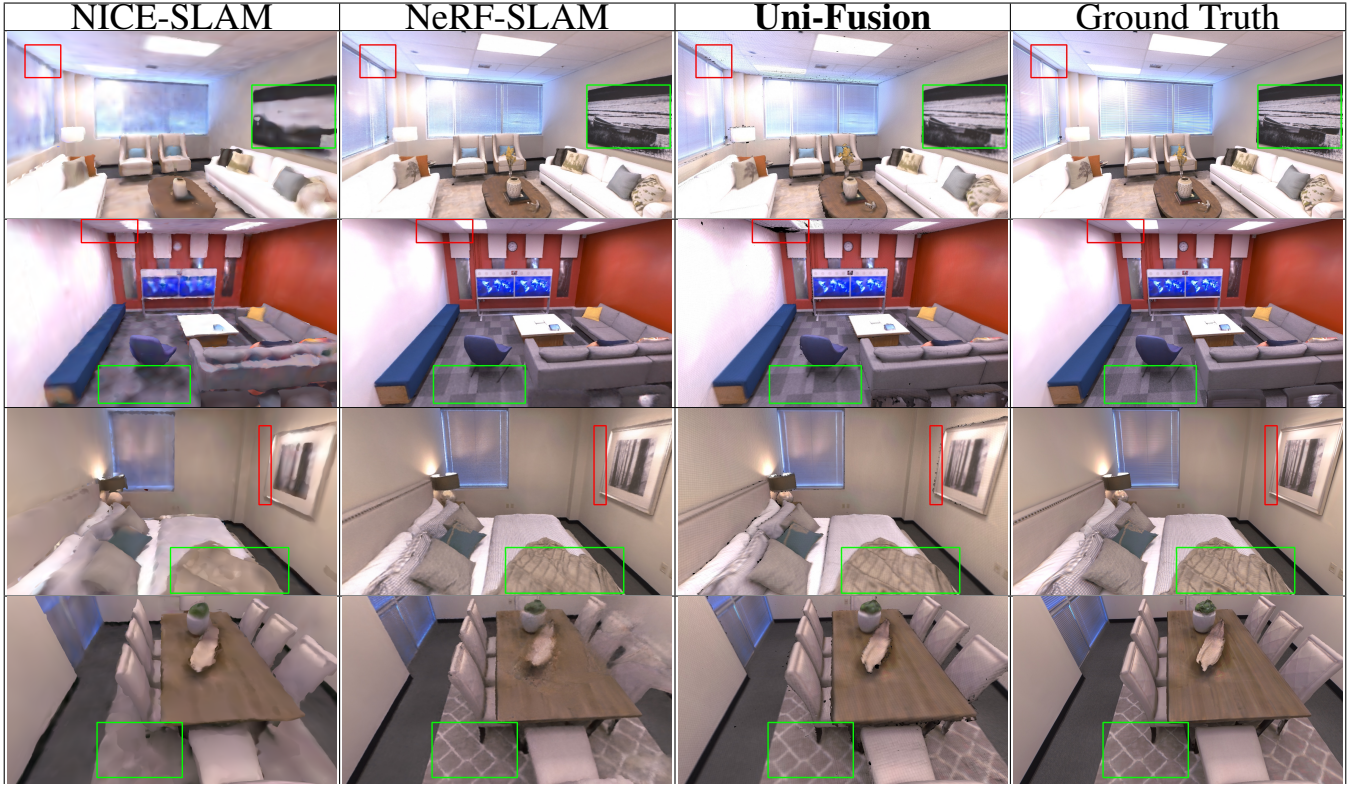


Fig. 10. Demonstration of color rendering on the Replica dataset. Fine appearances are highlighted in **green window**. Small flaws are in a **red box**.

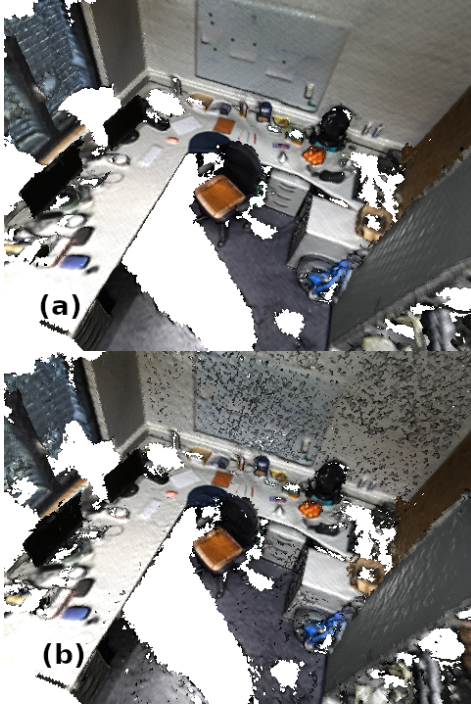


Fig. 11. Ablation study on surface construction basis. (a) Sample based. (b) Derivative based.

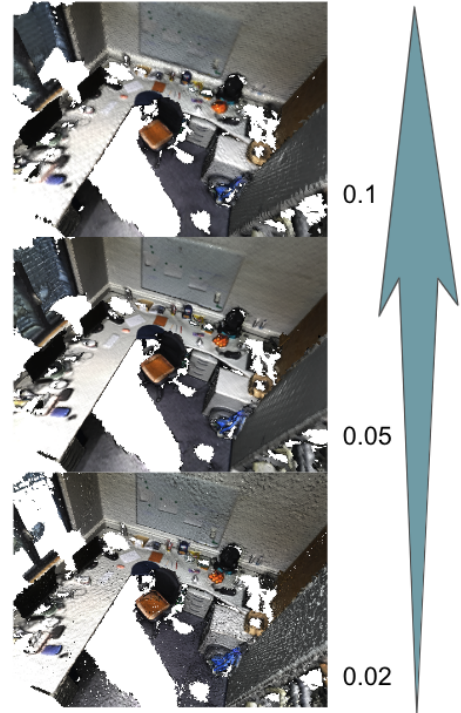


Fig. 12. Ablation study on voxel size.

of Yijun's office is demonstrated. Both models are able to construct, but the derivative-based model produces a lot of noise on the surface. This is because for smoothness purpose, we build voxels that are overlapped to its neighbor, which causes redundant voxels near the surface. For those redundant

voxels, no center sample is provided and thus the derivative based surface construction builds bad SDFs on unknown region of the voxels.

Instead, sample-based surface construction does not have this problem as it adds more points in voxels and is able to construct highly-smooth surfaces. From which, we find well constructed and colored white board, chair, school bag and even the oranges.

2) *Tracking*: Our Uni-Fusion use a coarse-to-fine strategy for tracking. An external tracking model is running in one thread aside from the mapping thread. In the mapping thread, it takes pose result from the external tracking and applies the internal tracking for colored point cloud.

The result is demonstrated in Table V. The coarse-to-fine is relatively better on trajectory estimation.

3) *Voxel size*: Testing the office scene, we vary the voxel size from low to high. From Fig. 12, when low voxel size 0.02m is used, the surface is rough. Then when voxel size goes larger, the smoothness is improved. However, when we use 0.1m voxel size, the surface color is blur. Considering Uni-Fusion produces a surface color field, the quality of surface directly affect the coloring. Thus, continuing enlarging the voxel size also results in worse surface results.

Therefore, in the above experiments, 0.05m voxel size is utilized for surface construction. In addition, each voxel for encoding are actually with size 0.1m, since we use overlapped voxel.

G. Results for 2D-to-3D transfer

Except for surface and color, Uni-Fusion also supports continuous mapping of other fabricated data. Therefore, we implement Uni-Fusion on style-transfer data and saliency data to approach a style- and saliency-transfer on the 3D canvas.

In Fig. 13, we demonstrate artistic painting in 3D canvas. We use MSG-Net [42] to transfer style for each fed frame

and use Uni-Fusion to construct the style LIM for the surface style field. The test scene is office0 of the Replica dataset from one view angle. 20 images are used to provide the style and are attached at bottom-left corner correspondingly. We see that our Uni-Fusion well-constructs style meshes in the taste of the provided style images. For example, with pure style or abstract painting, the 3D “canvas” demonstrates a very close style. Our favorite style is in the middle of the fourth row, it even produces a high quality 3D sketch painting.

In Fig. 14, we demonstrate saliency detection in 3D. In this figure we select three scenes from ScanNet and two scenes from Replica. Similarly, we detect saliency on each frame using InSPyReNet [57] and construct saliency LIM for surface saliency field.

In the second row, high salient regions are colored in yellow. Here we see the object that is interest. This further directs a robot in 3D scene. For example, in first column, sofa, chair, curtain and television in the room surely gets more attention in daily life. In the second, a meeting room, obviously the long desk and chairs are the major components. Also for the bed in the third column of the hotel room, the sofa, desk, lamp, television in the fourth and the sofas and chairs in the last.

H. Scene Understanding Results

The saliency detection highlights the interesting object well. This is considered part of 3D semantic understanding. However, the semantics may vary and we find it is inefficient to fuse different semantic information in multiple LIMs. Thus in this section, we use Uni-Fusion to fuse and build a surface field for high-dimensional CLIP-embeddings. In this way, with one LIM, we construct different semantic results for corresponding commands. Since now our Uni-Fusion works with OpenSeg for Scene Understanding purpose, we call it Uni-Fusion-SU.

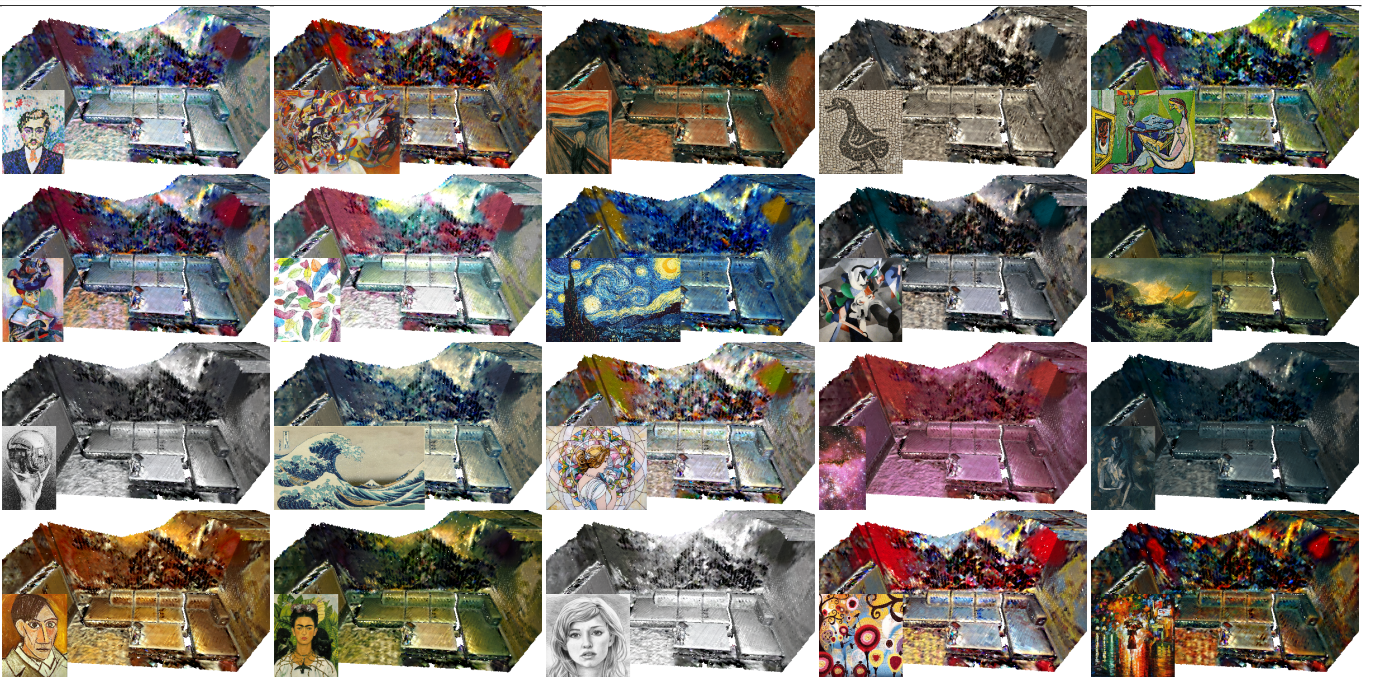


Fig. 13. Style transfer on 3D canvas.

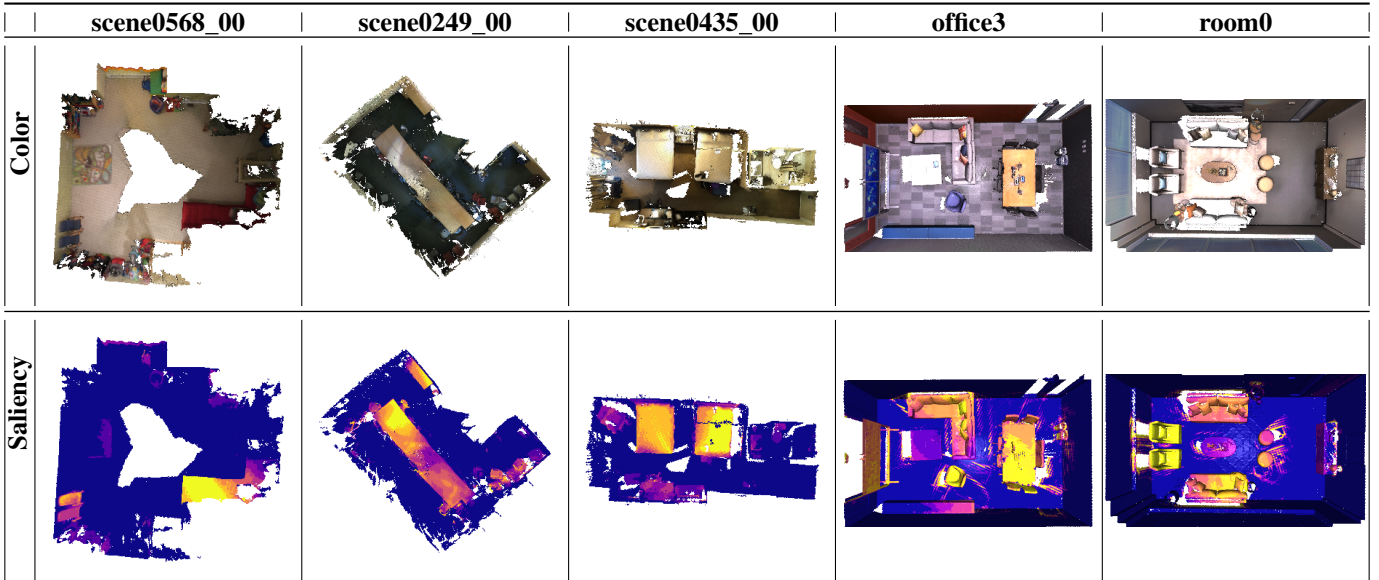


Fig. 14. Saliency transfer on the 3D canvas. The upper row is the result of the colored mesh. The lower row is saliency mesh.

1) *Semantic Segmentation*: We first evaluate model on generalized zero-shot point cloud semantic segmentation application. Generalized Zero-Shot Learning (GZSL) differs from Zero-Shot Learning (ZSL) that ZSL only predicts classes unseen at training time while GZSL predicts both unseen and seen [50]. Thus the comparison with GZSL SOTAs better reveals the potential of Uni-Fusion-SU as it does not train on both.

In this test, ScanNet and S3DIS datasets are involved for benchmarking. Note that, the **compared baselines are trained on the corresponding datasets**. Our Uni-Fusion-SU use OpenSeg to provide the 2D image level feature embedding. Thus though **Uni-Fusion-SU** is also Zero-shot, **it does not touch any ScanNet or S3DIS annotations**.

We demonstrate the mIoU scores in Table VI. Here, we see that our model achieves best result in Zero-shot learning methods on the ScanNet dataset. In addition, it is also competitive to fully-supervised methods.

We also list results on unseen classes in Table VII. Though not as good as the fully supervised result, Uni-Fusion-SU works much better than 3DGenZ. Especially, our Uni-Fusion-SU is highly precise on classes like sofa and Toilet comparing

to the even fully supervised model.

TABLE VII
CLASSWISE GZSL SEMANTIC SEGMENTATION PERFORMANCE (%) ON THE SCANNET UNSEEN SPLIT.

		Bookshelf	Desk	Sofa	Toilet	mean
FSL (Fully supervise)	IoU	56.9	30.0	57.4	63.4	51.9
3DGenZ (Zero-shot)	IoU	6.3	3.3	13.1	8.1	7.7
Uni-Fusion-SU (Ours)	IoU	38.3	16.8	51.7	60.9	41.9
3DGenZ (Zero-shot)	Acc.	13.4	5.9	49.6	26.3	23.8
Uni-Fusion-SU (Ours)	Acc.	61.9	29.6	67.4	91.6	62.6

However, in S3DIS, our model doesnot exceed 3DGenZ and others in Table VI.

Even in unseen data result in Table VIII, we find Uni-Fusion-SU hardly finds some class, e.g. Beam and Column, which is not a commonly annotated object. While for common object sofa and window, our result is still much higher.

We demonstrate the semantic segmentation result in Fig. 15. We find 3DGenZ's result is more noisy. This is shown in the spotted sofa, bed and etc. While Uni-Fusion-SU's result is overall smoother and precise.

TABLE VI
GZSL SEMANTIC SEGMENTATION RESULTS. SCORES ARE IN %. [†] INDICATE 3DGENZ'S ADAPTION OF THE METHOD. NOTE THAT, UNI-FUSION DOES NOT EVEN TRAIN WITH THE SEEN CLASSES.

	Training set		Inference input	ScanNet			S3DIS		
	Backbone	Classifier		<i>Seen</i>	<i>Unseen</i>	<i>All</i>	<i>Seen</i>	<i>Unseen</i>	<i>All</i>
<i>Supervised methods with different levels of supervision</i>									
Full supervision	<i>seen</i> \cup <i>unseen</i>	<i>seen</i> \cup <i>unseen</i>	Point Cloud	43.3	51.9	45.1	74.0	50.0	66.6
ZSL backbone	<i>seen</i>	<i>seen</i> \cup <i>unseen</i>	Point Cloud	41.5	39.2	40.3	60.9	21.5	48.7
ZSL-trivial	<i>seen</i>	<i>seen</i>	Point Cloud	39.2	0.0	31.3	70.2	0.0	48.6
<i>Generalized zero-shot-learning methods</i>									
ZSLPC-Seg [48] [†]	<i>seen</i>	<i>unseen</i>	Point Cloud	28.2	0.0	22.6	65.6	0.0	45.3
DeViSe-3DSeg [49] [†]	<i>seen</i>	<i>unseen</i>	Point Cloud	20.0	0.0	16.0	70.2	0.0	48.6
3DGenZ [50]	<i>seen</i>	<i>seen</i> \cup <i>unseen</i>	Point Cloud	32.8	7.7	27.8	53.1	7.3	39.0
<i>Zero-shot learning + map fusion</i>									
Uni-Fusion-SU (Ours)	None	None	Sparse Frames	31.0	41.9	32.9	31.3	24.0	29.0

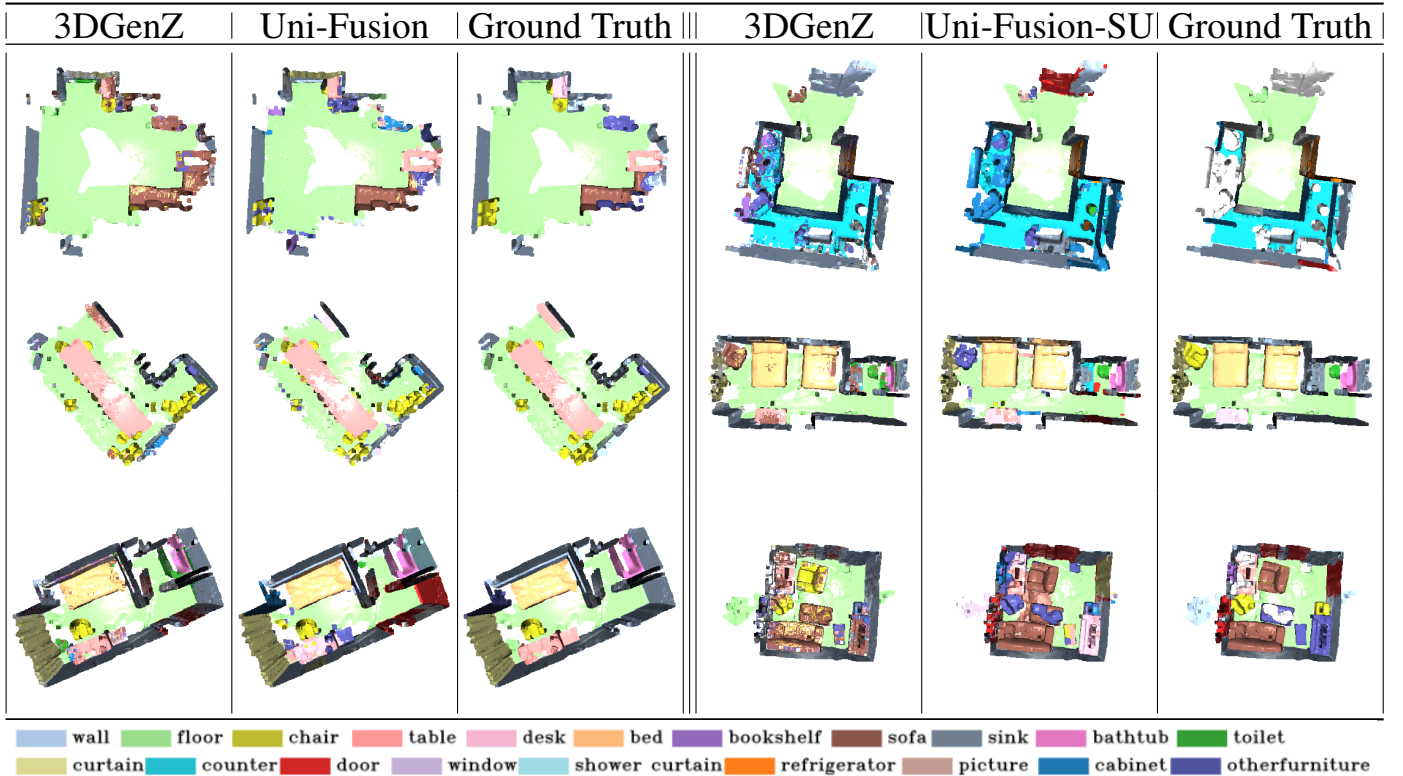


Fig. 15. Semantic segmentation demo on the ScanNet dataset. Selected scenes are consistent to Fig. 9

TABLE VIII
CLASSWISE GZSL SEMANTIC SEGMENTATION PERFORMANCE (%) ON THE S3DIS UNSEEN SPLIT.

		Beam	Column	Sofa	Window	mean
FSL (Fully supervise)	IoU	63.1	10.2	54.1	72.4	50.0
3DGenZ (Zero-shot)	IoU	13.9	2.4	4.9	8.1	7.3
Uni-Fusion-SU (Ours)	IoU	5.5	0.02	57.4	32.9	24.0
3DGenZ (Zero-shot)	Acc.	20.0	9.1	62.4	23.7	28.8
Uni-Fusion-SU (Ours)	Acc.	41.5	0.02	78.3	42.1	40.5

2) *Scene Understanding with Different Properties*: The main contribution of this application is that, Uni-Fusion is the first model that builds a continuous mapping of high-dimensional embedding on surface without any training. In above experiment (Section VI-H1), we evaluate the performance of generalized zero-shot semantic segmentation. But the potential is not limited to semantic segmentation. With a LIM constructed, a surface CLIP feature field is obtained. Then without the need of multiple LIMs or rerun for other properties, we query **Object, Room Type, Material, Affordance and Activity**.

We demonstrate results in Fig. 16, where we query object (desk, sofa), activity (work), affordance (sittable) and material (wood). Uni-Fusion-SU precisely finds the object and material region and highlights it. However, when the searching command is less accurate, such as work or sittable, it gives a wider range while in some place less confident (with dull yellow). The options are also roughly correct.

I. Time

We run all applications in one pass using our captured office sequences and evaluate the time cost for the construction and fusion of each LIM. The average time cost over frames are shown in Table IX.

TABLE IX
TIME REQUIRED IN SECONDS FOR EACH FRAME.

	Surface	Color	Infrared	Style	Saliency	Latent	Internal Track
Time (s)	0.100	0.038	0.045	0.048	0.045	0.011	0.225

From this table, with depth and properties images of size 720×1280 as input, our model works with a frequency of $\sim 10\text{Hz}$ for surface (sample mode) LIM construction and integration. While even $20 + \text{Hz}$ for color, infrared, style, and saliency. This shows our Uni-Fusion is adequate for real-time applications.

However, our internal tracking takes around 0.225s for a frame which is comparatively slower than the mapping module. Though, Uni-Fusion exploits an external tracking to protect the model from losing track, which enables our internal tracking and mapping to have a lower frequency. And thus the whole model is applicable to be real-time in various scenarios.

VII. EXTENSIVE EXPERIMENT ON OUR OWN DATASET

In previous experiments, we assessed the capabilities of our Uni-Fusion in various applications. For robotic understanding of the surroundings, we capture our own dataset to show all applications together.




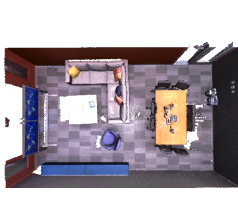
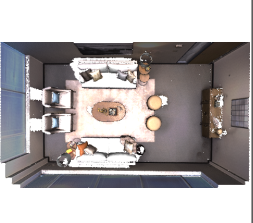

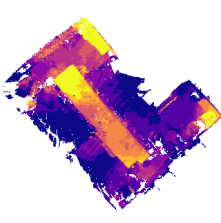

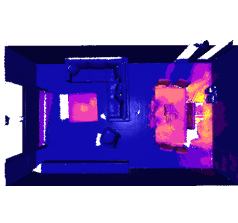
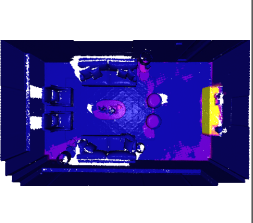



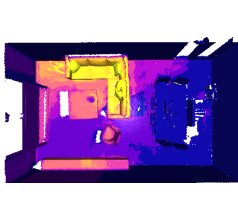
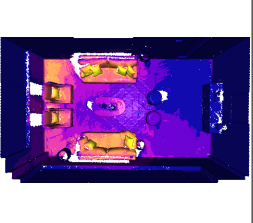

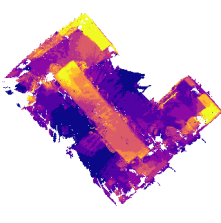
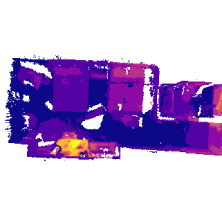
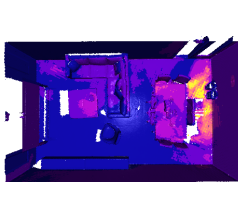
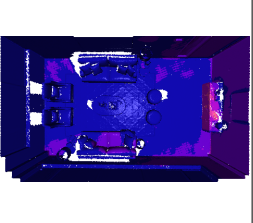

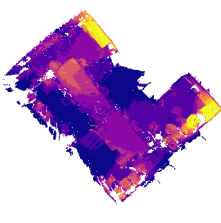

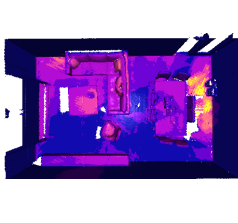
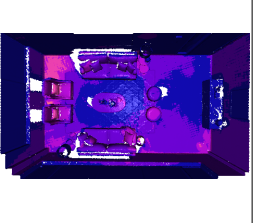
	scene0568_00	scene0249_00	scene0435_00	office3	room0
Desk					
Sofa					
Work					
Sittable					
Wood					

Fig. 16. Demonstration of the original mesh, highlighted semantic mesh given various queries.

We capture two scenes: The office and apartment of the first author using a Microsoft Kinect Azure. RGB-D and infrared video are captured. After calibration, RGB, depth, infrared inputs are with the resolution of 720×1280 . Uni-Fusion tracks and reconstructs all applications in one pass. Office data has been involved in ablation study Section VI-F. We demonstrate all applications on the apartment dataset that is shown in

Fig. 17.

Again, the ceiling of reconstruction is removed for better visualization. In the top row, we show the colored mesh with room details, infrared mesh which reveals the light affect, saliency reconstruction that indicates the objects that are important for navigation. Next, we choose the second style in Fig. 13 to transfer onto the apartment canvas. The wooden

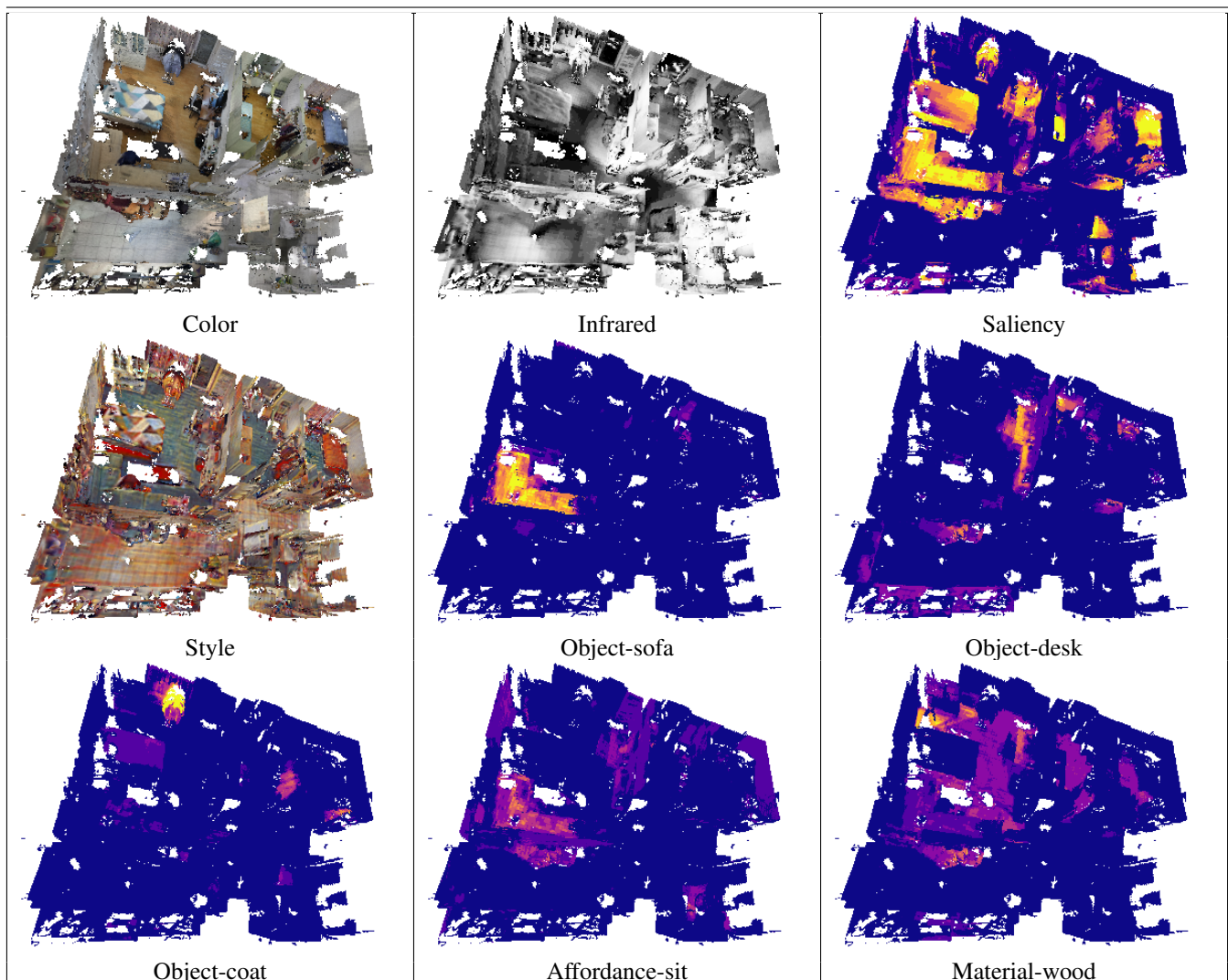


Fig. 17. Demonstration on the captured apartment data.

floor in the room is colored with dark green. The overall apartment is in a warm style.

The rest are generated from the surface field of the CLIP embeddings. We command object to find, e.g., where is the sofa, desk and coat. In addition, it easily finds affordances like sit-able. For material, it successfully finds the wooden floor in each room.

VIII. LIMITATIONS AND FUTURE WORKS

1) *Remapping*: Right now, Uni-Fusion does not support deintegrating local LIM from global LIM that is essential to include bundle adjustment (BA) or loop closing. More importantly, the local LIM does not support transformation of LIMs as NIM-REM [12] does it at the current stage. To foster a better qualities and higher computational performances and to support large scale mapping, loop closing and bundle adjustment are future targets.

2) *Visual Language Navigation*: Uni-Fusion provides a good reconstruction and scene understanding basis for Visual-Language Robot Navigation (VLN). Related works produces a 2D embedding map [39] while Uni-Fusion is capable to

construct a 3D embedding map with the scene. Thus Uni-Fusion can help the robot to have a richer understanding of the scene. In future work, we will investigate applications like navigation.

IX. CONCLUSION

In this work, we propose a novel universal model for all continuous mapping applications, namely Uni-Fusion. Without any training, Uni-Fusion constructs Latent Implicit Maps that support geometry and arbitrary properties. Moving one step further to scene understanding, Uni-Fusion is also the first model that is capable to construct continuous maps with high dimensional embeddings. With such a basis, we have implemented a high-quality incremental Surface&Color reconstruction application, a 2D-to-3D fabricated properties transfer application and an open-vocabulary scene understanding application.

ACKNOWLEDGEMENTS

This work was in parts supported by the Federal Ministry for Economic Affairs and Climate Action (BMWK) on the

basis of a decision by the German Bundestag und the grant number KK5150104GM1. We also acknowledge the support by the Elite Network Bavaria (ENB) through the “Satellite Technology” academic program..

REFERENCES

- [1] S. T. O’Callaghan and F. T. Ramos, “Gaussian process occupancy maps,” *The Intl. Journal of Robotics Research*, vol. 31, no. 1, pp. 42–62, 2012.
- [2] M. Ghaffari Jadidi, J. Valls Miro, and G. Dissanayake, “Gaussian processes autonomous mapping and exploration for range-sensing mobile robots,” *Autonomous Robots*, vol. 42, pp. 273–290, 2018.
- [3] Y. Yuan, H. Kuang, and S. Schwertfeger, “Fast gaussian process occupancy maps,” in *2018 15th Intl. Conf. on Control, Automation, Robotics and Vision (ICARCV)*. IEEE, 2018, pp. 1502–1507.
- [4] W. Martens, Y. Poffet, P. R. Soria, R. Fitch, and S. Sukkarieh, “Geometric priors for gaussian process implicit surfaces,” *IEEE Robotics and Automation Letters*, vol. 2, no. 2, pp. 373–380, 2016.
- [5] B. Lee, C. Zhang, Z. Huang, and D. D. Lee, “Online continuous mapping using gaussian process implicit surfaces,” in *2019 Intl. Conf. on Robotics and Automation (ICRA)*. IEEE, 2019, pp. 6884–6890.
- [6] L. Wu, K. M. B. Lee, L. Liu, and T. Vidal-Calleja, “Faithful euclidean distance field from log-gaussian process implicit surfaces,” *IEEE Robotics and Automation Letters*, vol. 6, no. 2, pp. 2461–2468, 2021.
- [7] J.-P. A. Ivan, T. Stoyanov, and J. A. Stork, “Online distance field priors for gaussian process implicit surfaces,” *IEEE Robotics and Automation Letters*, vol. 7, no. 4, pp. 8996–9003, 2022.
- [8] B. Curless and M. Levoy, “A volumetric method for building complex models from range images,” in *Proc. of the 23rd annual conf. on Computer graphics and interactive techniques*, 1996, pp. 303–312.
- [9] S. Izadi, D. Kim, O. Hilliges, D. Molyneaux, R. Newcombe, P. Kohli, J. Shotton, S. Hodges, D. Freeman, A. Davison *et al.*, “Kinectfusion: real-time 3d reconstruction and interaction using a moving depth camera,” in *Proc. of the 24th annual ACM symposium on User interface software and technology*, 2011, pp. 559–568.
- [10] A. Dai, M. Nießner, M. Zollhöfer, S. Izadi, and C. Theobalt, “Bundle-fusion: Real-time globally consistent 3d reconstruction using on-the-fly surface reintegration,” *ACM Transactions on Graphics (ToG)*, vol. 36, no. 4, p. 1, 2017.
- [11] J. Huang, S.-S. Huang, H. Song, and S.-M. Hu, “Di-fusion: Online implicit 3d reconstruction with deep priors,” in *Proc. of the IEEE/CVF Conf. on Computer Vision and Pattern Recognition*, 2021, pp. 8932–8941.
- [12] Y. Yuan and A. Nüchter, “An algorithm for the se (3)-transformation on neural implicit maps for remapping functions,” *IEEE Robotics and Automation Letters*, vol. 7, no. 3, pp. 7763–7770, 2022.
- [13] E. Sucar, S. Liu, J. Ortiz, and A. J. Davison, “imap: Implicit mapping and positioning in real-time,” in *Proc. of the IEEE/CVF Intl. Conf. on Computer Vision*, 2021, pp. 6229–6238.
- [14] Z. Zhu, S. Peng, V. Larsson, W. Xu, H. Bao, Z. Cui, M. R. Oswald, and M. Pollefeys, “Nice-slam: Neural implicit scalable encoding for slam,” in *Proc. of the IEEE/CVF Conf. on Computer Vision and Pattern Recognition*, 2022, pp. 12786–12796.
- [15] W. E. Lorensen and H. E. Cline, “Marching cubes: A high resolution 3d surface construction algorithm,” *ACM siggraph computer graphics*, vol. 21, no. 4, pp. 163–169, 1987.
- [16] K. Li, Y. Tang, V. A. Prisacariu, and P. H. Torr, “Bnv-fusion: Dense 3d reconstruction using bi-level neural volume fusion,” in *Proc. of the IEEE/CVF Conf. on Computer Vision and Pattern Recognition*, 2022, pp. 6166–6175.
- [17] A. Rosinol, J. J. Leonard, and L. Carlone, “Nerf-slam: Real-time dense monocular slam with neural radiance fields,” *arXiv preprint arXiv:2210.13641*, 2022.
- [18] G. Ghiasi, X. Gu, Y. Cui, and T.-Y. Lin, “Scaling open-vocabulary image segmentation with image-level labels,” in *Computer Vision–ECCV 2022: 17th European Conf., Tel Aviv, Israel, October 23–27, 2022, Proc., Part XXXVI*. Springer, 2022, pp. 540–557.
- [19] R. Senanayake and F. Ramos, “Bayesian hilbert maps for dynamic continuous occupancy mapping,” in *Conf. on Robot Learning*. PMLR, 2017, pp. 458–471.
- [20] W. Zhi, L. Ott, R. Senanayake, and F. Ramos, “Continuous occupancy map fusion with fast bayesian hilbert maps,” in *2019 Intl. Conf. on Robotics and Automation (ICRA)*. IEEE, 2019, pp. 4111–4117.
- [21] J. J. Park, P. Florence, J. Straub, R. Newcombe, and S. Lovegrove, “Deepsdf: Learning continuous signed distance functions for shape representation,” in *Proc. of the IEEE/CVF conf. on computer vision and pattern recognition*, 2019, pp. 165–174.
- [22] L. Mescheder, M. Oechsle, M. Niemeyer, S. Nowozin, and A. Geiger, “Occupancy networks: Learning 3d reconstruction in function space,” in *Proc. of the IEEE/CVF conf. on computer vision and pattern recognition*, 2019, pp. 4460–4470.
- [23] R. Chabra, J. E. Lenssen, E. Ilg, T. Schmidt, J. Straub, S. Lovegrove, and R. Newcombe, “Deep local shapes: Learning local sdf priors for detailed 3d reconstruction,” in *Computer Vision–ECCV 2020: 16th European Conf., Glasgow, UK, August 23–28, 2020, Proc., Part XXIX 16*. Springer, 2020, pp. 608–625.
- [24] C. Jiang, A. Sud, A. Makadia, J. Huang, M. Nießner, T. Funkhouser *et al.*, “Local implicit grid representations for 3d scenes,” in *Proc. of the IEEE/CVF Conf. on Computer Vision and Pattern Recognition*, 2020, pp. 6001–6010.
- [25] S. Peng, M. Niemeyer, L. Mescheder, M. Pollefeys, and A. Geiger, “Convolutional occupancy networks,” in *Computer Vision–ECCV 2020: 16th European Conf., Glasgow, UK, August 23–28, 2020, Proc., Part III 16*. Springer, 2020, pp. 523–540.
- [26] S. Lionar, L. Schmid, C. Cadena, R. Siegwart, and A. Cramariuc, “Neuralbox: Real-time neural representation fusion for robust volumetric mapping,” in *2021 Intl. Conf. on 3D Vision (3DV)*. IEEE, 2021, pp. 1279–1289.
- [27] Z. Deng, J. Shi, and J. Zhu, “Neuralef: Deconstructing kernels by deep neural networks,” *arXiv preprint arXiv:2205.00165*, 2022.
- [28] A. Rahimi and B. Recht, “Random features for large-scale kernel machines,” *Advances in neural information processing systems*, vol. 20, 2007.
- [29] —, “Weighted sums of random kitchen sinks: Replacing minimization with randomization in learning,” *Advances in neural information processing systems*, vol. 21, 2008.
- [30] F. X. X. Yu, A. T. Suresh, K. M. Choromanski, D. N. Holtmann-Rice, and S. Kumar, “Orthogonal random features,” *Advances in neural information processing systems*, vol. 29, 2016.
- [31] M. Munkhoeva, Y. Kapushev, E. Burnaev, and I. Oseledets, “Quadrature-based features for kernel approximation,” *Advances in neural information processing systems*, vol. 31, 2018.
- [32] D. P. Francis and K. Raimond, “Major advancements in kernel function approximation,” *Artificial Intelligence Review*, vol. 54, no. 2, pp. 843–876, 2021.
- [33] C. Williams and M. Seeger, “Using the nyström method to speed up kernel machines,” *Advances in neural information processing systems*, vol. 13, 2000.
- [34] T. Yang, Y.-F. Li, M. Mahdavi, R. Jin, and Z.-H. Zhou, “Nyström method vs random fourier features: A theoretical and empirical comparison,” *Advances in neural information processing systems*, vol. 25, 2012.
- [35] C. K. Williams and C. E. Rasmussen, *Gaussian processes for machine learning*. MIT press Cambridge, MA, 2006, vol. 2, no. 3.
- [36] E. Solak, R. Murray-Smith, W. Leithhead, D. Leith, and C. Rasmussen, “Derivative observations in gaussian process models of dynamic systems,” *Advances in neural information processing systems*, vol. 15, 2002.
- [37] J. Park, Q.-Y. Zhou, and V. Koltun, “Colored point cloud registration revisited,” in *Proc. of the IEEE intl. conf. on computer vision*, 2017, pp. 143–152.
- [38] S. Peng, K. Genova, C. Jiang, A. Tagliasacchi, M. Pollefeys, T. Funkhouser *et al.*, “Openscene: 3d scene understanding with open vocabularies,” *arXiv preprint arXiv:2211.15654*, 2022.
- [39] C. Huang, O. Mees, A. Zeng, and W. Burgard, “Visual language maps for robot navigation,” in *ICRA*, 2023.
- [40] A. Dai, A. X. Chang, M. Savva, M. Halber, T. Funkhouser, and M. Nießner, “Scannet: Richly-annotated 3d reconstructions of indoor scenes,” in *Proc. of the IEEE conf. on computer vision and pattern recognition*, 2017, pp. 5828–5839.
- [41] J. Sturm, N. Engelhard, F. Endres, W. Burgard, and D. Cremers, “A benchmark for the evaluation of rgb-d slam systems,” in *2012 IEEE/RSJ intl. conf. on intelligent robots and systems*. IEEE, 2012, pp. 573–580.
- [42] H. Zhang and K. Dana, “Multi-style generative network for real-time transfer,” in *Proc. of the European Conf. on Computer Vision (ECCV) Workshops*, 2018, pp. 0–0.
- [43] C. R. Qi, L. Yi, H. Su, and L. J. Guibas, “Pointnet++: Deep hierarchical feature learning on point sets in a metric space,” *Advances in neural information processing systems*, vol. 30, 2017.
- [44] I. Armeni, O. Sener, A. R. Zamir, H. Jiang, I. Brilakis, M. Fischer, and S. Savarese, “3d semantic parsing of large-scale indoor spaces,” in *Proc.*

- of the *IEEE conf. on computer vision and pattern recognition*, 2016, pp. 1534–1543.
- [45] Occipital, “Occipital: The structure sensor,” 2016.
 - [46] I. Armeni, S. Sax, A. R. Zamir, and S. Savarese, “Joint 2d-3d-semantic data for indoor scene understanding,” *arXiv preprint arXiv:1702.01105*, 2017.
 - [47] A. Rosinol, J. J. Leonard, and L. Carlone, “Probabilistic volumetric fusion for dense monocular slam,” in *Proc. of the IEEE/CVF Winter Conf. on Applications of Computer Vision*, 2023, pp. 3097–3105.
 - [48] A. Cheraghian, S. Rahman, and L. Petersson, “Zero-shot learning of 3d point cloud objects,” in *2019 16th Intl. Conf. on Machine Vision Applications (MVA)*. IEEE, 2019, pp. 1–6.
 - [49] A. Frome, G. S. Corrado, J. Shlens, S. Bengio, J. Dean, M. Ranzato, and T. Mikolov, “Devise: A deep visual-semantic embedding model,” *Advances in neural information processing systems*, vol. 26, 2013.
 - [50] B. Michele, A. Boulch, G. Puy, M. Bucher, and R. Marlet, “Generative zero-shot learning for semantic segmentation of 3d point clouds,” in *2021 Intl. Conf. on 3D Vision (3DV)*. IEEE, 2021, pp. 992–1002.
 - [51] Q.-Y. Zhou, J. Park, and V. Koltun, “Open3d: A modern library for 3d data processing,” *arXiv preprint arXiv:1801.09847*, 2018.
 - [52] T. Schops, T. Sattler, and M. Pollefeys, “Bad slam: Bundle adjusted direct rgb-d slam,” in *Proc. of the IEEE/CVF Conf. on Computer Vision and Pattern Recognition*, 2019, pp. 134–144.
 - [53] T. Whelan, M. Kaess, M. Fallon, H. Johannsson, J. Leonard, and J. McDonald, “Kintinuous: Spatially extended kinectfusion,” 2012.
 - [54] R. Mur-Artal and J. D. Tardós, “Orb-slam2: An open-source slam system for monocular, stereo, and rgb-d cameras,” *IEEE transactions on robotics*, vol. 33, no. 5, pp. 1255–1262, 2017.
 - [55] Z. Teed and J. Deng, “Droid-slam: Deep visual slam for monocular, stereo, and rgb-d cameras,” *Advances in neural information processing systems*, vol. 34, pp. 16 558–16 569, 2021.
 - [56] T. Müller, A. Evans, C. Schied, and A. Keller, “Instant neural graphics primitives with a multiresolution hash encoding,” *ACM Transactions on Graphics (ToG)*, vol. 41, no. 4, pp. 1–15, 2022.
 - [57] T. Kim, K. Kim, J. Lee, D. Cha, J. Lee, and D. Kim, “Revisiting image pyramid structure for high resolution salient object detection,” in *Proc. of the Asian Conf. on Computer Vision*, 2022, pp. 108–124.